

NUCLEAR CONSTRAINTS ON PROPERTIES OF NEUTRON STAR CRUSTS

JUN XU^{1,2}, LIE-WEN CHEN^{1,3}, BAO-AN LI⁴, AND HONG-RU MA¹

¹ Institute of Theoretical Physics, Shanghai Jiao Tong University, Shanghai 200240, China; xujun@comp.tamu.edu, hrma@sjtu.edu.cn

² Cyclotron Institute and Physics Department, Texas A&M University, College Station, TX 77843-3366, USA

³ Center of Theoretical Nuclear Physics, National Laboratory of Heavy-Ion Accelerator, Lanzhou 730000, China; lwchen@sjtu.edu.cn

⁴ Department of Physics, Texas A&M University-Commerce, Commerce, TX 75429-3011, USA; Bao-An_Li@tamu-commerce.edu

Received 2009 January 12; accepted 2009 March 16; published 2009 May 13

ABSTRACT

The transition density ρ_t and pressure P_t at the inner edge separating the liquid core from the solid crust of neutron stars are systematically studied using a modified Gogny (MDI) and 51 popular Skyrme interactions within well established dynamical and thermodynamical methods. First of all, it is shown that the widely used parabolic approximation to the full equation of state (EOS) of isospin asymmetric nuclear matter may lead to huge errors in estimating the transition density and pressure, especially for stiffer symmetry energy functionals $E_{\text{sym}}(\rho)$, compared to calculations using the full EOS within both the dynamical and thermodynamical methods mainly because of the energy curvatures involved. Thus, fine details of the EOS of asymmetric nuclear matter are important for locating accurately the inner edge of the neutron star crust. Second, the transition density and pressure decrease roughly linearly with increasing slope parameter L of $E_{\text{sym}}(\rho)$ at normal nuclear matter density using the full EOS within both the dynamical and thermodynamical methods. It is also shown that the thickness, fractional mass, and moment of inertia of the neutron star crust are all very sensitive to the parameter L through the transition density ρ_t whether one uses the full EOS or its parabolic approximation. Moreover, it is shown that $E_{\text{sym}}(\rho)$ constrained in the same subsaturation density range as the neutron star crust by the isospin diffusion data in heavy-ion collisions at intermediate energies limits the transition density and pressure to $0.040 \text{ fm}^{-3} \leq \rho_t \leq 0.065 \text{ fm}^{-3}$ and $0.01 \text{ MeV fm}^{-3} \leq P_t \leq 0.26 \text{ MeV fm}^{-3}$, respectively. These constrained values for the transition density and pressure are significantly lower than their fiducial values currently used in the literature. Furthermore, the mass–radius relation and several other properties closely related to the neutron star crust are studied by using the MDI interaction. It is found that the newly constrained ρ_t and P_t together with the earlier estimate of $\Delta I/I > 0.014$ for the crustal fraction of the moment of inertia of the Vela pulsar impose a more stringent constraint of $R \geq 4.7 + 4.0M/M_\odot \text{ km}$ for the radius R and mass M of neutron stars compared to previous studies in the literature.

Key words: dense matter – equation of state – stars: neutron

Online-only material: color figures

1. INTRODUCTION

Neutron stars are among the most mysterious objects in the universe. They are natural testing grounds of our knowledge about the equation of state (EOS) of neutron-rich nuclear matter. The latter determines the structure and many properties of neutron stars (Lattimer & Prakash 2007; Oyamatsu & Iida 2007; Douchin & Haensel 2000; Horowitz & Piekarewicz 2001; Kubis 2004, 2007; Ducoin et al. 2007; Rabhi et al. 2009). Neutron stars are expected to have a solid inner crust which is believed to play an important role in understanding a number of astrophysical observations (Baym et al. 1971a, 1971b; Pethick & Ravenhall 1995; Pethick et al. 1995; Lattimer & Prakash 2000, 2001, 2007; Steiner et al. 2005a; Chamel & Haensel 2008) such as pulsar glitches (Link et al. 1999), quasi-periodic oscillations observed in X-ray emission following X-ray bursts on a neutron star (Duncan 1998), the cooling observed over the first several years following superbursts from neutron stars or giant flares from magnetars (Rutledge et al. 2006), and neutrino opacities (Horowitz et al. 2004; Burrows et al. 2006). The solid inner crust of a neutron star comprises the region between the density ρ_{out} where neutrons drip out of nuclei and the density ρ_t where the transition to homogeneous nucleonic matter occurs. While ρ_{out} is relatively well determined to be $\rho_{\text{out}} \approx 4 \times 10^{11} \text{ g cm}^{-3}$ (Ruster et al. 2006; Hempel & Schaffner-Bielich 2008), the transition density ρ_t is still very uncertain (Lattimer & Prakash 2000, 2001, 2007). This

is largely due to our poor knowledge about the EOS of neutron-rich nuclear matter, especially the density dependence of the nuclear symmetry energy $E_{\text{sym}}(\rho)$ at subsaturation densities (Lattimer & Prakash 2000, 2001, 2007). Consequently, our ability to understand accurately many important properties of neutron stars has been hampered (Lattimer & Prakash 2000, 2001, 2004, 2007).

The EOS of neutron-rich nuclear matter also plays an important role in heavy-ion collisions, especially those induced by neutron-rich radioactive beams in terrestrial laboratories. While heavy-ion collisions are not expected to create the same matter and conditions as in neutron stars, the same elementary nuclear interactions are at work in the two cases. Thus it is important to examine the ramifications of conclusions regarding the EOS extracted from one field in the other one. Significant progress has been made recently in constraining the EOS of neutron-rich nuclear matter using heavy-ion experiments (see, e.g., Li et al. 2008 for the most recent review). In particular, compared to the existing model predictions in the literature the analyses of isospin diffusion data (Tsang et al. 2004; Chen et al. 2005a; Li & Chen 2005) in heavy-ion collisions have constrained relatively tightly $E_{\text{sym}}(\rho)$ in exactly the same subsaturation density region around the expected inner edge of neutron star crust. Moreover, conclusions from analyzing some recent data (Shetty et al. 2007) of the isoscaling phenomenon (Tsang et al. 2001) in heavy-ion collisions and the available data on the thickness of the neutron skin in ^{208}Pb (Steiner & Li 2005b; Li & Chen 2005;

Chen et al. 2005b) are consistent with the $E_{\text{sym}}(\rho)$ constrained by the isospin diffusion data. Furthermore, the lower bound of the experimentally constrained $E_{\text{sym}}(\rho)$ is consistent with the relativistic mean field model prediction using the FSUGold interaction that can reproduce not only saturation properties of nuclear matter but also structure properties and giant resonances of many finite nuclei (Piekraewicz 2007). While some model dependence and uncertainties still exist in the analyses of the above-mentioned experiments and calculations, an overlapping area of the extracted $E_{\text{sym}}(\rho)$ from several analyses has appeared in the subsaturation density region (Tsang et al. 2009; Lynch et al. 2009). On the other hand, extremely impressive progress has also been made in astrophysical observations relevant for constraining the EOS of nuclear matter. To our best knowledge, nevertheless, mainly because of the low precision associated with the current measurements of neutron star radii, a noncontroversial conclusion on the EOS and the density dependence of the symmetry energy has yet to come. More accurate observations of neutron stars' properties, especially their radii, with advanced X-ray satellites and other observatories will hopefully enable us to constrain stringently the EOS of neutron-rich matter in the near future. A direct crosscheck on the EOS extracted independently from heavy-ion reactions and neutron star observations will then be possible. In the meantime, examinations of astrophysical implications of the EOS constrained by heavy-ion reactions are useful. At the WCI3 meeting in 2005, Horowitz suggested that the heavy-ion physics community should investigate whether one can use information from heavy-ion collisions to constrain the core–crust transition density in neutron stars (Horowitz 2005). It is thus timely to investigate how the behavior of $E_{\text{sym}}(\rho)$ constrained at subsaturation densities by heavy-ion experiments may help limit the transition density ρ_t and pressure P_t at the inner edge of neutron stars (Xu et al. 2009).

To our best knowledge, all existing studies indicate consistently that the transition density is very sensitive to the density dependence of the nuclear symmetry energy (Lattimer & Prakash 2007; Oyamatsu & Iida 2007; Douchin & Haensel 2000; Kubis 2004, 2007). Very often, the so-called parabolic approximation (PA) to the EOS of isospin asymmetric nuclear matter is used. While the PA is mathematically valid only at small isospin asymmetries, interestingly it has been found to be true empirically even for large isospin asymmetries for nucleonic matter using most models and interactions (see, e.g., Bombaci & Lombardo 1991; Chen et al. 2001; Zuo et al. 2004; Xu et al. 2007a; van Dalena et al. 2007; Mou 2007). Nevertheless, since the npe matter in the crust at β -equilibrium is highly neutron rich and the determination of the transition density depends on the second-order derivatives of the energy density, the fine details of the EOS can influence the transition density significantly as first pointed out by Arponen (1972). It is thus interesting and necessary to compare calculations using both the full EOS and its parabolic approximation. Indeed, we found that the PA leads to significantly different transition density and pressure compared to the calculations using the full EOS. It should be mentioned that the PA may also significantly modify the proton fraction in β -equilibrium neutron star matter and the critical density for the direct Urca process which can lead to faster cooling of neutron stars (Zhang & Chen 2001; Steiner 2006). To investigate effects of nuclear interactions we use a modified Gogny (MDI) and 51 Skyrme interactions widely used in the literature. The same MDI interaction has been used in extracting $E_{\text{sym}}(\rho)$ from heavy-ion reactions within a transport model (Chen et al. 2005a;

Li & Chen 2005). Using the $E_{\text{sym}}(\rho)$ constrained by the isospin diffusion data (Tsang et al. 2004), we can put a constraint on the transition density and pressure, respectively. We will then examine the implications of these constraints on the mass–radius correlation and the crustal fraction of the moment of inertia of neutron stars.

This paper is organized as follows. In Section 2, we briefly review the dynamical and thermodynamical methods widely used for locating the inner edge of neutron star crust, and derive their relationship analytically. In Section 3, we summarize the EOS and symmetry energy obtained using the MDI interaction and 51 Skyrme interactions within the Hartree–Fock approach. We also examine the associated proton fraction and several thermodynamical properties including the energy density, pressure, and the speed of sound in neutron star matter at β -equilibrium. The general formalisms for describing the structure of neutron stars are outlined in Section 4. We then present the results of our calculations and discuss several important issues regarding the transition density and the structure of neutron stars in Section 5. A summary is given in Section 6.

2. METHODS FOR LOCATING THE INNER EDGE OF NEUTRON STAR CRUST

The inner edge of neutron star crust corresponds to the phase transition from homogeneous matter at high densities to inhomogeneous matter at low densities. In principle, the transition density ρ_t can be obtained by comparing a detailed model of the nonuniform solid crust to the uniform liquid core in the neutron star. While this is practically very difficult since the inner crust may have a very complex structure, usually known as “nuclear pasta” (Ravenhall et al. 1983; Hashimoto et al. 1984; Lorenz et al. 1993; Oyamatsu 1993; Horowitz et al. 2004; Steiner 2008; Gogelein et al. 2008; Avancini et al. 2008, 2009), it can be explored within several approaches including molecular dynamics simulations (Watanabe 2005; Horowitz 2006) and the three-dimensional Hartree–Fock model (William & Newton 2009, private communication). Furthermore, the core–crust transition is thought to be a very weak first-order phase transition and model calculations lead to very small density discontinuities at the transition (Pethick et al. 1995; Douchin & Haensel 2000, 2001; Carriere et al. 2003). Alternatively, a well established approach for estimating ρ_t is to search for the density at which the uniform liquid first becomes unstable against small-amplitude density fluctuations, indicating the start of forming nuclear clusters. Although some quantum effects such as the shell effects in more microscopic methods may influence the core–crust transition density, this approach has been shown to produce a very small error for the actual core–crust transition density and it would yield the exact transition density for a second-order phase transition (Pethick et al. 1995; Douchin & Haensel 2000, 2001; Carriere et al. 2003). Presently, there are several such methods, such as the dynamical method (Baym et al. 1971a, 1971b; Pethick & Ravenhall 1995; Pethick et al. 1995; Douchin & Haensel 2000; Oyamatsu & Iida 2007; Ducoin et al. 2007), the thermodynamical method (Kubis 2004, 2007; Lattimer & Prakash 2007; Worley et al. 2008a), and the random phase approximation (RPA) (Horowitz & Piekraewicz 2001; Carriere et al. 2003). In the present work, we use both the dynamical and thermodynamical methods.

In the following, we will first review briefly the dynamical method and the thermodynamical method separately. While they are both well established and applied extensively in studying not only the core–crust transition in neutron stars but also the

liquid–gas phase transition in asymmetric nuclear matter, somewhat different results are often obtained. It is thus necessary to study in detail the differences and relations between them. We shall first show analytically that the thermodynamical method corresponds to the long-wavelength limit of the dynamical method when the Coulomb interaction is neglected, and then compare numerically their predictions.

2.1. The Dynamical Method

To describe small density fluctuations in the npe matter, one can write the density of particle $q \in \{n, p, e\}$ as (Baym et al. 1971a; Pethick et al. 1995; Ducoin et al. 2007)

$$\rho_q = \rho_q^0 + \delta\rho_q. \quad (1)$$

The density variation can be decoupled into plane waves

$$\delta\rho_q = A_q e^{i\vec{k}\cdot\vec{r}} + c.c., \quad (2)$$

of wavevector \vec{k} and amplitude A_q . This kind of density variation occurs when a momentum \vec{k} is transferred to the particle system, e.g., through collisions, and the “dynamical method” is named after this. It has been shown that the variation of the free-energy density generated by the density fluctuation of amplitude $\tilde{A} = (A_n, A_p, A_e)$ can be written as (Baym et al. 1971a; Pethick et al. 1995; Ducoin et al. 2007)

$$\delta f = \tilde{A}^* \mathcal{C}^f \tilde{A}, \quad (3)$$

where

$$\mathcal{C}^f = \begin{pmatrix} \partial\mu_n/\partial\rho_n & \partial\mu_n/\partial\rho_p & 0 \\ \partial\mu_p/\partial\rho_n & \partial\mu_p/\partial\rho_p & 0 \\ 0 & 0 & \partial\mu_e/\partial\rho_e \end{pmatrix} + k^2 \begin{pmatrix} D_{nn} & D_{np} & 0 \\ D_{pn} & D_{pp} & 0 \\ 0 & 0 & 0 \end{pmatrix} + \frac{4\pi e^2}{k^2} \begin{pmatrix} 0 & 0 & 0 \\ 0 & 1 & -1 \\ 0 & -1 & 1 \end{pmatrix} \quad (4)$$

is the free-energy curvature matrix. The instability region of the npe matter can be located by examining when the convexity of the free-energy curvature matrix is violated. The convexity of the matrix \mathcal{C}^f requires that

$$C_{11}^f > 0 \text{ or } C_{22}^f > 0, \quad \begin{vmatrix} C_{11}^f & C_{12}^f \\ C_{21}^f & C_{22}^f \end{vmatrix} > 0, \quad \begin{vmatrix} C_{11}^f & C_{12}^f & C_{13}^f \\ C_{21}^f & C_{22}^f & C_{23}^f \\ C_{31}^f & C_{32}^f & C_{33}^f \end{vmatrix} > 0. \quad (5)$$

Here C_{33}^f is always positive, so we do not take it into consideration. If the system stays stable, the convexity of the matrix \mathcal{C}^f should be retained for all values of k . The first term on the right-hand side of Equation (4) is the bulk term, which just defines the stability condition of the nuclear matter part as will be shown later. The second term on the right-hand side of Equation (4) describes the contribution of the density gradient. For the Skyrme–Hartree–Fock (SHF) model (Chabanat et al. 1997), one has

$$D_{nn} = D_{pp} = \frac{3}{16} [t_1(1 - x_1) - t_2(1 + x_2)], \quad (6)$$

$$D_{np} = D_{pn} = \frac{1}{16} [3t_1(2 + x_1) - t_2(2 + x_2)], \quad (7)$$

in terms of the standard Skyrme interaction parameters x_1 , x_2 , t_1 , and t_2 . The MDI interaction, however, does not have a gradient term. To remedy this drawback, we set $D_{pp} = D_{nn} = D_{np} = 132 \text{ MeV fm}^5$ as used in the work by Oyamatsu et al. (Oyamatsu & Iida 2007) when we apply the MDI interaction. This choice is quite consistent with the empirical values from the SHF calculations. We note here that the averaged values of $D_{pp} = D_{nn}$ and $D_{np} = D_{pn}$ are, respectively, 140.9 and 118.8 MeV fm^5 for the 51 Skyrme forces we will use in the following. Furthermore, as we will show later, the transition density and pressure are rather insensitive to the variation of $D_{pp} = D_{nn}$ and $D_{np} = D_{pn}$. The last term on the right-hand side of Equation (4) is the Coulomb term, which is generated by the Coulomb interactions of electrons and protons. It should be noted that additional k -dependent terms due to the finite range of the MDI interaction via exchange terms as well as the Coulomb exchange terms are neglected in Equation (4). As we will show later, the bulk term dominates the result, and the density gradient term and Coulomb term are not important for the determination of the transition density and the associated transition pressure. The density gradient and Coulomb terms usually make the system slightly more stable and thus reduce correspondingly the region of instability.

For small density fluctuations, to guarantee the convexity of the curvature matrix it is sufficient for the last determinant in Equation (5) to be positive (Baym et al. 1971b; Pethick et al. 1995), i.e.,

$$V_{\text{dyn}}(k) \approx V_0 + \beta k^2 + \frac{4\pi e^2}{k^2 + k_{TF}^2} > 0, \quad (8)$$

where

$$V_0 = \frac{\partial\mu_p}{\partial\rho_p} - \frac{(\partial\mu_n/\partial\rho_p)^2}{\partial\mu_n/\partial\rho_n}, \quad (9)$$

$$\beta = D_{pp} + 2D_{np}\zeta + D_{nn}\zeta^2,$$

$$\zeta = -\frac{\partial\mu_p/\partial\rho_n}{\partial\mu_n/\partial\rho_n}, \quad (10)$$

$$k_{TF}^2 = \frac{4\pi e^2}{\partial\mu_e/\partial\rho_e}. \quad (11)$$

In the above expressions, we used the relation $\frac{\partial\mu_n}{\partial\rho_p} = \frac{\partial\mu_p}{\partial\rho_n}$ following $\frac{\partial\mu_n}{\partial\rho_p} = \frac{\partial}{\partial\rho_p} \left(\frac{\partial\varepsilon}{\partial\rho_n} \right) = \frac{\partial}{\partial\rho_n} \left(\frac{\partial\varepsilon}{\partial\rho_p} \right) = \frac{\partial\mu_p}{\partial\rho_n}$, with ε being the energy density of the npe matter. Meanwhile, $\frac{\partial\mu_n}{\partial\rho_n}$ is assumed to be positive. If we have $\frac{\partial\mu_n}{\partial\rho_n} < 0$ but $\frac{\partial\mu_p}{\partial\rho_p} > 0$, we can change the form of the equations correspondingly. In this form, it is clear that the density gradient and the Coulomb term clearly contribute positively to $V_{\text{dyn}}(k)$. They thus help to make the system more stable. At $k = \left[\left(\frac{4\pi e^2}{\beta} \right)^{1/2} - k_{TF}^2 \right]^{1/2}$, $V_{\text{dyn}}(k)$ has a minimal value of (Baym et al. 1971b; Pethick et al. 1995)

$$V_{\text{dyn}} = V_0 + 2(4\pi e^2 \beta)^{1/2} - \beta k_{TF}^2. \quad (12)$$

Then the density at which Equation (12) becomes zero determines the instability boundary.

2.2. The Thermodynamical Method

The thermodynamical method requires the system to obey the stability condition (Kubis 2004, 2007; Lattimer & Prakash 2007)

$$-\left(\frac{\partial P}{\partial v} \right)_\mu > 0, \quad (13)$$

$$-\left(\frac{\partial\mu}{\partial q_c}\right)_v > 0, \quad (14)$$

or the system will be unstable against small density fluctuations. These conditions are equivalent to requiring the convexity of the energy per particle in the single phase (Kubis 2004, 2007; Lattimer & Prakash 2007) by ignoring the finite size effects due to surface and Coulomb energies as shown in the following. Here the $P = P_b + P_e$ is the total pressure of the npe system with the contributions P_b and P_e from baryons and electrons, respectively. The v and q_c are the volume and charge per baryon number. μ is the chemical potential defined as

$$\mu = \mu_n - \mu_p. \quad (15)$$

In fact, Equation (13) is simply the well known mechanical stability condition of the system at a fixed μ . It ensures that any local density fluctuation will not diverge. On the other hand, Equation (14) is the charge or chemical stability condition of the system at a fixed density. It means that any local charge variation violating the charge neutrality condition will not diverge. If the β -equilibrium condition is satisfied, namely $\mu = \mu_e$, the electron contribution to the pressure P_e is only a function of the chemical potential μ , and in this case one can rewrite Equation (13) as

$$-\left(\frac{\partial P_b}{\partial v}\right)_\mu > 0. \quad (16)$$

By using the relation $\frac{\partial E_b(\rho, x_p)}{\partial x_p} = -\mu$, one can get (Kubis 2004, 2007)

$$\begin{aligned} -\left(\frac{\partial P_b}{\partial v}\right)_\mu &= 2\rho^3 \frac{\partial E_b(\rho, x_p)}{\partial \rho} + \rho^4 \frac{\partial^2 E_b(\rho, x_p)}{\partial \rho^2} \\ &\quad - \rho^4 \left(\frac{\partial^2 E_b(\rho, x_p)}{\partial \rho \partial x_p}\right)^2 / \frac{\partial^2 E_b(\rho, x_p)}{\partial x_p^2}, \end{aligned} \quad (17)$$

$$-\left(\frac{\partial q_c}{\partial \mu}\right)_v = 1 / \frac{\partial^2 E_b(\rho, x_p)}{\partial x_p^2} + \frac{\partial \rho_e}{\partial \mu_e} / \rho, \quad (18)$$

where $q_c = x_p - \rho_e / \rho$. $\rho = 1/v$ is the baryon density, and $E_b(\rho, x_p)$ is the energy per baryon. Within the free Fermi gas model, the density of electrons ρ_e is uniquely determined by the electron chemical potential μ_e . Then the thermodynamical relations Equations (13) and (14) are identical to (Lattimer & Prakash 2007; Kubis 2004, 2007)

$$\begin{aligned} -\left(\frac{\partial P_b}{\partial v}\right)_\mu &= \rho^2 \left[2\rho \frac{\partial E_b(\rho, x_p)}{\partial \rho} + \rho^2 \frac{\partial^2 E_b(\rho, x_p)}{\partial \rho^2} \right. \\ &\quad \left. - \left(\frac{\partial^2 E_b(\rho, x_p)}{\partial \rho \partial x_p}\right)^2 / \frac{\partial^2 E_b(\rho, x_p)}{\partial x_p^2} \right] > 0, \end{aligned} \quad (19)$$

$$-\left(\frac{\partial q_c}{\partial \mu}\right)_v = 1 / \frac{\partial^2 E_b(\rho, x_p)}{\partial x_p^2} + \frac{\mu_e^2}{\pi^2 \hbar^3 \rho} > 0, \quad (20)$$

respectively. The second inequality is usually valid. Thus, the following condition from the first one determines the

thermodynamical instability region:

$$\begin{aligned} V_{\text{ther}} &= 2\rho \frac{\partial E_b(\rho, x_p)}{\partial \rho} + \rho^2 \frac{\partial^2 E_b(\rho, x_p)}{\partial \rho^2} \\ &\quad - \left(\frac{\partial^2 E_b(\rho, x_p)}{\partial \rho \partial x_p}\right)^2 / \frac{\partial^2 E_b(\rho, x_p)}{\partial x_p^2}. \end{aligned} \quad (21)$$

Within the parabolic approximation, neglecting higher-order terms of isospin asymmetry $\delta = 1 - 2x_p$, the EOS of asymmetric nuclear matter is

$$E_b(\rho, \delta) = E_0(\rho) + E_{\text{sym}}(\rho)\delta^2, \quad (22)$$

where $E_0(\rho)$ is the energy per nucleon of symmetric nuclear matter. Then Equation (21) can be re-expressed as (Lattimer & Prakash 2007)

$$\begin{aligned} V_{\text{ther}}^{PA} &= \rho^2 \frac{d^2 E_0}{d\rho^2} + 2\rho \frac{dE_0}{d\rho} + (1 - 2x_p)^2 \\ &\quad \times \left[\rho^2 \frac{d^2 E_{\text{sym}}}{d\rho^2} + 2\rho \frac{dE_{\text{sym}}}{d\rho} - 2E_{\text{sym}}^{-1} \left(\rho \frac{dE_{\text{sym}}}{d\rho} \right)^2 \right]. \end{aligned} \quad (23)$$

2.3. The Relationship between the Dynamical and Thermodynamical Methods

Equations (12) and (21) together with the relationship between the density ρ and the proton fraction x_p required by the β -equilibrium and the charge neutrality conditions will then determine, respectively, the dynamical and the thermodynamical core-crust transition density in neutron stars. These two methods together with various EOSs have been widely used in the literature, while their relationship is still unclear. Therefore, it would be interesting to first obtain some analytical insights on their relationship before comparing their numerical predictions.

In the following, we first analyze the instability of asymmetric nuclear matter without considering the β -equilibrium and the charge neutrality conditions. As used in the previous subsection and the literature, the stability condition is often expressed using the ρ and x_p within the dynamical method, but $\rho_n = (1 - x_p)\rho$ and $\rho_p = x_p\rho$ within the thermodynamical one. Thus the following simple thermodynamical relations are useful for understanding the relationship between the two methods:

$$\frac{\partial E_b}{\partial x_p} = -\mu = \mu_p - \mu_n, \quad (24)$$

$$\frac{\partial P_b}{\partial \rho} = (1 - x_p)\rho \frac{\partial \mu_n}{\partial \rho} + x_p\rho \frac{\partial \mu_p}{\partial \rho}, \quad (25)$$

$$\frac{\partial P_b}{\partial x_p} = (1 - x_p)\rho \frac{\partial \mu_n}{\partial x_p} + x_p\rho \frac{\partial \mu_p}{\partial x_p}, \quad (26)$$

where the pressure of baryons is $P_b = \mu_n \rho_n + \mu_p \rho_p - E_b \rho$. In this way, the derivatives of the energy of baryons can be expressed as

$$\frac{\partial E_b}{\partial \rho} = \frac{P_b}{\rho^2}, \quad (27)$$

$$\begin{aligned}
\frac{\partial^2 E_b}{\partial \rho^2} &= \frac{\partial}{\partial \rho} \left(\frac{P_b}{\rho^2} \right) \\
&= -\frac{2P_b}{\rho^3} + \frac{1}{\rho^2} \left[(1-x_p)\rho \frac{\partial \mu_n}{\partial \rho} + x_p \rho \frac{\partial \mu_p}{\partial \rho} \right] \\
&= -\frac{2P_b}{\rho^3} + \frac{1}{\rho^2} \left[(1-x_p)^2 \rho \frac{\partial \mu_n}{\partial \rho_n} + x_p(1-x_p)\rho \frac{\partial \mu_n}{\partial \rho_p} \right] \\
&\quad + \frac{1}{\rho^2} \left[x_p(1-x_p)\rho \frac{\partial \mu_p}{\partial \rho_n} + x_p^2 \rho \frac{\partial \mu_p}{\partial \rho_p} \right], \quad (28)
\end{aligned}$$

$$\begin{aligned}
\frac{\partial^2 E_b}{\partial x_p^2} &= -\frac{\partial \mu}{\partial x_p} = \frac{\partial \mu_p}{\partial x_p} - \frac{\partial \mu_n}{\partial x_p} \\
&= \rho \left(\frac{\partial \mu_p}{\partial \rho_p} - \frac{\partial \mu_p}{\partial \rho_n} - \frac{\partial \mu_n}{\partial \rho_p} + \frac{\partial \mu_n}{\partial \rho_n} \right), \quad (29)
\end{aligned}$$

$$\begin{aligned}
\frac{\partial^2 E_b}{\partial \rho \partial x_p} &= -\frac{\partial \mu}{\partial \rho} = \frac{\partial \mu_p}{\partial \rho} - \frac{\partial \mu_n}{\partial \rho} \\
&= (1-x_p) \frac{\partial \mu_p}{\partial \rho_n} + x_p \frac{\partial \mu_p}{\partial \rho_p} - (1-x_p) \frac{\partial \mu_n}{\partial \rho_n} - x_p \frac{\partial \mu_n}{\partial \rho_p}. \quad (30)
\end{aligned}$$

As shown earlier, for nuclear matter without considering the Coulomb interaction one has

$$\frac{\partial \mu_n}{\partial \rho_p} = \frac{\partial \mu_p}{\partial \rho_n}. \quad (31)$$

From Equations (27)–(31), we can then obtain the following important equality:

$$\frac{2}{\rho} \frac{\partial E_b}{\partial \rho} \frac{\partial^2 E_b}{\partial x_p^2} + \frac{\partial^2 E_b}{\partial \rho^2} \frac{\partial^2 E_b}{\partial x_p^2} - \left(\frac{\partial^2 E_b}{\partial \rho \partial x_p} \right)^2 = \frac{\partial \mu_n}{\partial \rho_n} \frac{\partial \mu_p}{\partial \rho_p} - \left(\frac{\partial \mu_n}{\partial \rho_p} \right)^2. \quad (32)$$

Therefore, for positive values of $\frac{\partial^2 E_b}{\partial x_p^2}$, the condition (Equation (19)) is simply equivalent to requiring a positive bulk term V_0 in Equation (4). Since the transition density is usually in the subsaturation density region where $\frac{\partial^2 E_b}{\partial x_p^2} > 0$ is valid for almost all model EOSs, the thermodynamical stability condition is thus simply the limit of the dynamical one as $k \rightarrow 0$ (long-wavelength limit) when the Coulomb interaction is neglected.

3. THE EOS AND SYMMETRY ENERGY WITH SELECTED 51 SKYRME FORCES AND A MODIFIED GOGNY INTERACTION

In this section, we summarize the EOS and the corresponding symmetry energy obtained using the modified finite-range Gogny effective interaction (MDI; Das et al. 2003) and 51 popular Skyrme forces within the Hartree–Fock approach. These results will be used later in our numerical calculations of the core–crust transition density and pressure. The MDI interaction has been extensively used in our previous studies of heavy-ion collisions, the liquid–gas phase transition in asymmetric nuclear matter, and several issues in astrophysics (Li et al. 2008). The EOSs using various Skyrme forces are well known for their simple forms and successful descriptions of many interesting phenomenon (see, e.g., Chabanat et al. 1997;

Steiner et al. 2005a; Stone et al. 2003; Stone & Reinhard 2007). A very useful feature of both the MDI and the Skyrme interaction is that analytical expressions for many interesting physical quantities in asymmetric nuclear matter at zero temperature can be obtained.

3.1. The EOS and Symmetry Energy with Selected 51 Skyrme Interactions

Within the SHF approach, the energy per nucleon for symmetric nuclear matter can be expressed as (Chabanat et al. 1997)

$$\begin{aligned}
E_0(\rho) &= \frac{3\hbar^2}{10m} \left(\frac{3\pi^2}{2} \right)^{2/3} \rho^{2/3} + \frac{3}{8} t_0 \rho \\
&\quad + \frac{3}{80} \Theta_s \left(\frac{3\pi^2}{2} \right)^{2/3} \rho^{5/3} + \frac{1}{16} t_3 \rho^{\sigma+1}, \quad (33)
\end{aligned}$$

with $\Theta_s = 3t_1 + (5 + 4x_2)t_2$. For asymmetric nuclear matter, the energy per nucleon is (Chabanat et al. 1997)

$$\begin{aligned}
E_b(\rho, \delta \text{ or } x_p) &= \frac{3\hbar^2}{10m} \left(\frac{3\pi^2}{2} \right)^{2/3} \rho^{2/3} F_{5/3} + \frac{1}{8} t_0 \rho [2(x_0 + 2) \\
&\quad - (2x_0 + 1)F_2] + \frac{1}{48} t_3 \rho^{\sigma+1} [2(x_3 + 2) \\
&\quad - (2x_3 + 1)F_2] + \frac{3}{40} \left(\frac{3\pi^2}{2} \right)^{2/3} \rho^{5/3} \\
&\quad \times \left\{ [t_1(x_1 + 2) + t_2(x_2 + 2)] F_{5/3} \right. \\
&\quad \left. + \frac{1}{2} [t_2(2x_2 + 1) - t_1(2x_1 + 1)] F_{8/3} \right\}, \quad (34)
\end{aligned}$$

with

$$F_m(\delta) = \frac{1}{2} [(1 + \delta)^m + (1 - \delta)^m],$$

$$F_m(x_p) = 2^{m-1} [x_p^m + (1 - x_p)^m].$$

Within the parabolic approximation widely used in the literature, the symmetry energy is calculated from

$$E_{\text{sym}}(\rho) \approx E_b(\rho, \delta = 1) - E_b(\rho, \delta = 0). \quad (35)$$

But, strictly speaking, the symmetry energy should be the coefficient of δ^2 in the Taylor expansion of $E_b(\rho, \delta)$ in terms of δ , i.e.,

$$E_{\text{sym}}(\rho) = \frac{1}{2} \left(\frac{\partial^2 E_b}{\partial \delta^2} \right)_{\delta=0}. \quad (36)$$

We note here that the above two definitions for the symmetry energy would be the same should there be no higher-order terms in δ in the EOS of asymmetric nuclear matter (but it should be noted that the kinetic part of the EOS of asymmetric nuclear matter always contains higher-order terms in δ).

Thus, by definition of Equation (36), for Skyrme interactions, one has

$$\begin{aligned}
E_{\text{sym}}(\rho) &= \frac{1}{2} \left(\frac{\partial^2 E_b}{\partial \delta^2} \right)_{\delta=0} \\
&= \frac{\hbar^2}{6m} \left(\frac{3\pi^2}{2} \right)^{2/3} \rho^{2/3} - \frac{1}{8} t_0 (2x_0 + 1) \rho \\
&\quad - \frac{1}{24} \left(\frac{3\pi^2}{2} \right)^{2/3} \Theta_{\text{sym}} \rho^{5/3} - \frac{1}{48} t_3 (2x_3 + 1) \rho^{\sigma+1}, \quad (37)
\end{aligned}$$

Table 1
Parameters of the 51 Skyrme Forces

SHF	ρ_0^a	$E_0(\rho_0)^b$	K_0^c	$E_{\text{sym}}(\rho_0)^d$	L^e	K_{sym}^f
BSk3	0.157	-15.8	234.8	27.9	6.8	-306.9
BSk1	0.157	-15.8	231.3	27.8	7.2	-281.8
BSk2	0.157	-15.8	233.7	28.0	8.0	-297.0
MSk7	0.157	-15.8	231.2	27.9	9.4	-274.6
BSk4	0.157	-15.8	236.8	28.0	12.5	-265.9
BSk8	0.159	-15.8	230.3	28.0	14.9	-220.9
BSk6	0.157	-15.8	229.1	28.0	16.8	-215.2
BSk7	0.157	-15.8	229.3	28.0	18.0	-209.4
SKP	0.163	-16.0	201.0	30.0	19.6	-266.8
BSk5	0.157	-15.8	237.2	28.7	21.4	-240.3
SKXm	0.159	-16.0	238.1	31.2	32.1	-242.8
RATP	0.160	-16.0	239.4	29.2	32.4	-191.2
SKX	0.155	-16.1	271.1	31.1	33.2	-252.1
SKXce	0.155	-15.9	268.2	30.1	33.5	-238.4
BSk15	0.159	-16.0	241.6	30.0	33.6	-194.3
BSk16	0.159	-16.1	241.7	30.0	34.9	-187.4
BSk10	0.159	-15.9	238.8	30.0	37.2	-194.9
SGII	0.158	-15.6	214.7	26.8	37.6	-145.9
BSk12	0.159	-15.9	238.1	30.0	38.0	-191.4
BSk11	0.159	-15.9	238.1	30.0	38.4	-189.8
BSk13	0.159	-15.9	238.1	30.0	38.8	-187.9
BSk9	0.159	-15.9	231.4	30.0	39.9	-145.3
SLy10	0.158	-16.5	237.8	33.2	40.8	-148.0
BSk14	0.159	-15.9	239.3	30.0	43.9	-152.0
SLy230a	0.160	-16.0	229.9	32.0	44.3	-98.2
SKM*	0.160	-15.8	216.6	30.0	45.8	-155.9
SLy230b	0.160	-16.0	229.9	32.0	46.0	-119.7
SLy6	0.161	-16.5	237.9	32.2	46.7	-117.0
SLy8	0.163	-16.6	238.0	32.4	46.8	-121.0
SLy4	0.162	-16.6	238.0	32.8	46.9	-124.6
SLy0	0.163	-16.6	238.3	32.4	46.9	-121.4
SLy3	0.163	-16.6	238.0	33.1	47.0	-126.9
SKM	0.160	-15.8	216.6	30.7	49.3	-148.8
SLy7	0.161	-16.5	237.8	33.4	49.7	-118.9
SLy2	0.162	-16.5	237.3	33.3	50.3	-117.9
SLy1	0.163	-16.6	237.9	33.5	50.4	-120.2
SLy5	0.163	-16.6	238.0	33.6	51.9	-116.3
SLy9	0.153	-16.4	237.7	33.2	57.2	-84.9
Sk16	0.159	-15.9	248.2	29.9	59.2	-46.8
Sk14	0.160	-15.9	248.0	29.5	60.4	-40.6
SGI	0.154	-15.9	261.8	28.3	63.9	-52.0
SKO*	0.160	-15.7	222.1	32.1	69.7	-77.5
SkMP	0.159	-16.1	238.5	30.1	70.7	-51.4
SKa	0.155	-16.0	263.2	32.9	74.6	-78.5
SKO	0.160	-15.8	222.8	32.0	79.5	-42.3
R $_{\sigma}$	0.158	-15.6	237.4	30.6	85.7	-9.1
SKT4	0.157	-15.5	229.3	34.8	92.4	-24.2
G $_{\sigma}$	0.158	-15.6	237.2	31.4	94.0	14.0
SkI3	0.158	-16.0	258.2	34.8	100.5	73.0
SkI2	0.158	-15.8	240.9	33.4	104.3	70.7
SkI5	0.156	-15.8	255.8	36.6	129.3	159.6

Notes.

^a ρ_0 : saturation density (fm^{-3}).

^b $E_0(\rho_0)$: binding energy of symmetric nuclear matter (MeV).

^c K_0 : incompressibility (MeV).

^d $E_{\text{sym}}(\rho_0)$: symmetry energy (MeV).

^e L : slope of the symmetry energy at the saturation density (MeV).

^f K_{sym} : curvature of the symmetry energy at the saturation density (MeV).

where $\Theta_{\text{sym}} = 3t_1x_1 - t_2(4 + 5x_2)$. σ , $t_0 \sim t_3$, and $x_0 \sim x_3$ are the Skyrme parameters.

As used extensively by many authors, near the saturation density ρ_0 , the symmetry energy can be expanded as

$$E_{\text{sym}}(\rho) \approx E_{\text{sym}}(\rho_0) + \frac{L}{3} \left(\frac{\rho - \rho_0}{\rho_0} \right) + \frac{K_{\text{sym}}}{18} \left(\frac{\rho - \rho_0}{\rho_0} \right)^2, \quad (38)$$

where L and K_{sym} are, respectively, the slope parameter and curvature parameter of the symmetry energy at ρ_0 , i.e.,

$$L = 3\rho_0 \left. \frac{\partial E_{\text{sym}}(\rho)}{\partial \rho} \right|_{\rho=\rho_0}, \quad (39)$$

$$K_{\text{sym}} = 9\rho_0^2 \left. \frac{\partial^2 E_{\text{sym}}(\rho)}{\partial \rho^2} \right|_{\rho=\rho_0}. \quad (40)$$

L and K_{sym} can be used conveniently to characterize the density dependence of the symmetry energy around the saturation density ρ_0 . In the present work, we use 51 standard Skyrme forces with their saturation density and the symmetry energy satisfying $0.140 \text{ fm}^{-3} < \rho_0 < 0.165 \text{ fm}^{-3}$ and $26 \text{ MeV} < E_{\text{sym}}(\rho_0) < 37 \text{ MeV}$, respectively. Some Skyrme forces with very small or negative L values are not considered here, as they generally predict bound pure neutron matter at subsaturation densities and are not suitable for the description of neutron-rich environments like neutron star crusts as discussed in detail by Stone et al. (2003). In addition, we have not included the Skyrme forces that predict values for the incompressibility K_0 inconsistent with the empirical value of about $240 \pm 40 \text{ MeV}$. The detailed values of the parameters for these 51 Skyrme forces are available from numerous references (Brack et al. 1985; Friedrich & Reinhard 1986; Brown 1998; Chabanat et al. 1997; Stone et al. 2003; Stone & Reinhard 2007; Chen et al. 2005b; Steiner & Li 2005b; Samyn et al. 2002, 2003, 2004, 2005; Goriely et al. 2003, 2005, 2006, 2007; Chamel et al. 2008; Goriely & Pearson 2008). The selected ranges of ρ_0 and $E_{\text{sym}}(\rho_0)$ are consistent with their empirical values inferred from nuclear laboratory data. The detailed properties of these forces at ρ_0 are summarized in Table 1 in the order of rising values of L .

3.2. The EOS and Symmetry Energy with the Modified Gogny Interaction MDI

For the MDI interaction based on the Hartree–Fock calculation using the Gogny interaction, the baryon potential energy density can be expressed as (Das et al. 2003)

$$V(\rho, \delta) = \frac{A_u(x)\rho_n\rho_p}{\rho_0} + \frac{A_l(x)}{2\rho_0}(\rho_n^2 + \rho_p^2) + \frac{B}{\sigma + 1} \frac{\rho^{\sigma+1}}{\rho_0^\sigma} (1 - x\delta^2) + \frac{1}{\rho_0} \sum_{\tau, \tau'} C_{\tau, \tau'} \int \int d^3p d^3p' \frac{f_{\tau}(\vec{r}, \vec{p}) f_{\tau'}(\vec{r}, \vec{p}')}{1 + (\vec{p} - \vec{p}')^2/\Lambda^2}. \quad (41)$$

We note here that the above is a natural extension to the isospin asymmetric case of the corresponding potential energy density for symmetric nuclear matter given by Gale et al. (1987), Prakash et al. (1988), Welke et al. (1988), Gale et al. (1990). It is similar to the Bombaci–Gale–Bertsch–Das Gupta (BGBD), and potential energy density (Bombaci 2001). The MDI interaction has been used extensively in studying heavy-ion reactions (Li et al. 2008), liquid–gas phase transitions in neutron-rich matter (Xu et al. 2007a, 2008; Li et al. 2007), and several structural properties (Li & Steiner 2006; Krastev & Li 2007; Krastev et al. 2008a) and gravitational wave emissions (Krastev et al. 2008b; Worley et al. 2008b) of neutron stars.

In the mean field approximation, Equation (41) leads to the following single particle potential for a nucleon with momentum

\vec{p} and isospin τ :

$$\begin{aligned}
U(\rho, \delta, \vec{p}, \tau) = & A_u(x) \frac{\rho_{-\tau}}{\rho_0} + A_l(x) \frac{\rho_\tau}{\rho_0} + B \left(\frac{\rho}{\rho_0} \right)^\sigma (1 - x\delta^2) \\
& - 8\tau x \frac{B}{\sigma + 1} \frac{\rho^{\sigma-1}}{\rho_0^\sigma} \delta \rho_{-\tau} + \frac{2C_{\tau, \tau}}{\rho_0} \\
& \times \int d^3 p' \frac{f_\tau(\vec{r}, \vec{p}')}{1 + (\vec{p} - \vec{p}')^2 / \Lambda^2} + \frac{2C_{\tau, -\tau}}{\rho_0} \\
& \times \int d^3 p' \frac{f_{-\tau}(\vec{r}, \vec{p}')}{1 + (\vec{p} - \vec{p}')^2 / \Lambda^2}. \quad (42)
\end{aligned}$$

In the above, the isospin $\tau = 1/2$ ($-1/2$) for neutrons (protons). The coefficients $A_u(x)$ and $A_l(x)$ are (Chen et al. 2005a)

$$A_u(x) = -95.98 - x \frac{2B}{\sigma + 1}, \quad A_l(x) = -120.57 + x \frac{2B}{\sigma + 1}. \quad (43)$$

The values of the parameters are $\sigma = 4/3$, $B = 106.35$ MeV, $C_{\tau, \tau} = -11.70$ MeV, $C_{\tau, -\tau} = -103.40$ MeV and $\Lambda = p_f^0$, which is the Fermi momentum of nuclear matter at ρ_0 (Das et al. 2003). The parameter x was introduced to mimic various $E_{\text{sym}}(\rho)$ predicted by different microscopic many-body theories. By adjusting the parameter x , $E_{\text{sym}}(\rho)$ is varied without changing any property of symmetric nuclear matter and the symmetry energy at saturation density, as the x -dependent $A_u(x)$ and $A_l(x)$ are automatically adjusted accordingly. We note especially that the symmetry energy at normal density $E_{\text{sym}}(\rho_0)$ is fixed independent of the parameter x . Using the definition in Equation (36), $E_{\text{sym}}(\rho_0) = 30.54$ MeV at $\rho_0 = 0.16$ fm $^{-3}$, while its value is 31.6 MeV within the parabolic approximation of Equation (35).

At zero temperature, the phase-space distribution function can be written as $f_\tau(\vec{r}, \vec{p}) = \frac{2}{h^3} \Theta(p_f(\tau) - p)$, and all the integral expressions can be calculated analytically (Welke et al. 1988; Das et al. 2003; Chen et al. 2007):

$$\begin{aligned}
& \int d^3 p' \frac{f_\tau(\vec{r}, \vec{p}')}{1 + (\vec{p} - \vec{p}')^2 / \Lambda^2} \\
& = \frac{2}{h^3} \pi \Lambda^3 \left[\frac{p_f^2(\tau) + \Lambda^2 - p^2}{2p\Lambda} \ln \frac{[p + p_f(\tau)]^2 + \Lambda^2}{[p - p_f(\tau)]^2 + \Lambda^2} \right. \\
& \left. + \frac{2p_f(\tau)}{\Lambda} - 2 \left\{ \arctan \frac{p + p_f(\tau)}{\Lambda} - \arctan \frac{p - p_f(\tau)}{\Lambda} \right\} \right], \quad (44)
\end{aligned}$$

$$\begin{aligned}
& \int \int d^3 p d^3 p' \frac{f_\tau(\vec{r}, \vec{p}) f_{\tau'}(\vec{r}, \vec{p}')}{1 + (\vec{p} - \vec{p}')^2 / \Lambda^2} \\
& = \frac{1}{6} \left(\frac{4\pi}{h^3} \right)^2 \Lambda^2 \left\{ p_f(\tau) p_f(\tau') [3(p_f^2(\tau) + p_f^2(\tau')) - \Lambda^2] \right. \\
& \quad + 4\Lambda \left[(p_f^3(\tau) - p_f^3(\tau')) \arctan \frac{p_f(\tau) - p_f(\tau')}{\Lambda} \right. \\
& \quad \left. - (p_f^3(\tau) + p_f^3(\tau')) \arctan \frac{p_f(\tau) + p_f(\tau')}{\Lambda} \right] \\
& \quad \left. + \frac{1}{4} [\Lambda^4 + 6\Lambda^2(p_f^2(\tau) + p_f^2(\tau')) - 3(p_f^2(\tau) - p_f^2(\tau'))^2] \right. \\
& \quad \left. \times \ln \frac{(p_f(\tau) + p_f(\tau'))^2 + \Lambda^2}{(p_f(\tau) - p_f(\tau'))^2 + \Lambda^2} \right\}. \quad (45)
\end{aligned}$$

The kinetic energy is

$$\begin{aligned}
E_k(\rho, \delta) = & \frac{1}{\rho} \int d^3 p \left(\frac{p^2}{2m} f_n(\vec{r}, \vec{p}) + \frac{p^2}{2m} f_p(\vec{r}, \vec{p}) \right) \\
& = \frac{4\pi}{5mh^3\rho} (p_{fn}^5 + p_{fp}^5), \quad (46)
\end{aligned}$$

where $p_{fn(p)} = \hbar(3\pi^2\rho_{n(p)})^{1/3}$ is the Fermi momentum of neutrons (protons). Then the total energy per baryon for cold asymmetric nuclear matter is

$$E_b(\rho, \delta) = \frac{V(\rho, \delta)}{\rho} + E_k(\rho, \delta). \quad (47)$$

By setting $\rho_n = \rho_p = \frac{\rho}{2}$ and $p_{fn} = p_{fp} = p_f$, we thus obtain the following EOS of cold symmetric nuclear matter:

$$\begin{aligned}
E_0(\rho) = & \frac{8\pi}{5mh^3\rho} p_f^5 + \frac{\rho}{4\rho_0} (A_l(x) + A_u(x)) \\
& + \frac{B}{\sigma + 1} \left(\frac{\rho}{\rho_0} \right)^\sigma + \frac{1}{3\rho_0\rho} (C_l + C_u) \left(\frac{4\pi}{h^3} \right)^2 \Lambda^2 \\
& \times \left[p_f^2 (6p_f^2 - \Lambda^2) - 8\Lambda p_f^3 \arctan \frac{2p_f}{\Lambda} \right. \\
& \left. + \frac{1}{4} (\Lambda^4 + 12\Lambda^2 p_f^2) \ln \frac{4p_f^2 + \Lambda^2}{\Lambda^2} \right]. \quad (48)
\end{aligned}$$

We stress here that since $A_l(x) + A_u(x)$ is a constant of -216.55 MeV according to Equation (43), $E_0(\rho)$ is independent of the parameter x as expected. The symmetry energy by definition is

$$\begin{aligned}
E_{\text{sym}}(\rho) = & \frac{1}{2} \left(\frac{\partial^2 E}{\partial \delta^2} \right)_{\delta=0} \\
& = \frac{8\pi}{9mh^3\rho} p_f^5 + \frac{\rho}{4\rho_0} (A_l(x) - A_u(x)) - \frac{Bx}{\sigma + 1} \left(\frac{\rho}{\rho_0} \right)^\sigma \\
& + \frac{C_l}{9\rho_0\rho} \left(\frac{4\pi}{h^3} \right)^2 \Lambda^2 \left[4p_f^4 - \Lambda^2 p_f^2 \ln \frac{4p_f^2 + \Lambda^2}{\Lambda^2} \right] \\
& + \frac{C_u}{9\rho_0\rho} \left(\frac{4\pi}{h^3} \right)^2 \Lambda^2 \left[4p_f^4 - p_f^2 (4p_f^2 + \Lambda^2) \ln \frac{4p_f^2 + \Lambda^2}{\Lambda^2} \right], \quad (49)
\end{aligned}$$

where $p_f = \hbar(3\pi^2\frac{\rho}{2})^{1/3}$ is the Fermi momentum for symmetric nuclear matter. We note here that since $A_l(x) - A_u(x) = -24.59 + 4Bx/(\sigma + 1)$ according to Equation (43), $E_{\text{sym}}(\rho)$ depends linearly on the parameter x at a given density except ρ_0 , where the symmetry energy is fixed by construction. As shown in Figure 1, adjusting the parameter x in the MDI interaction leads to a broad range of density dependence of nuclear symmetry energy, similar to those predicted by various microscopic and/or phenomenological many-body theories.

3.3. Thermodynamics Quantities in Neutron Stars at β -Equilibrium with the MDI Interaction

Since we are going to examine astrophysical implications of the symmetry energy constrained by heavy-ion reactions obtained from transport model analyses using the MDI interaction, it is useful to first study several key thermodynamical quantities

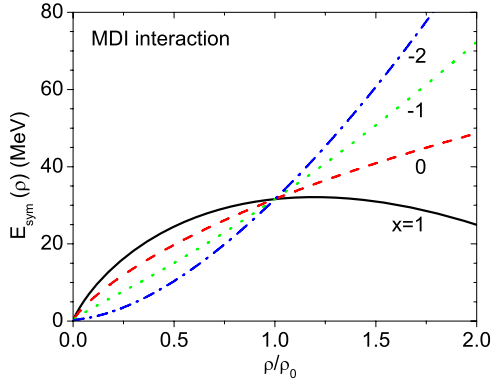


Figure 1. Density dependence of the nuclear symmetry energy for different values of the parameter x in the MDI interaction. Taken from Chen et al. (2005a).

(A color version of this figure is available in the online journal.)

in neutron star matter at β -equilibrium with charge neutrality. It is also necessary to examine the causality with the MDI interaction.

It is well known that for the $npe\mu$ matter, the β -equilibrium condition is

$$\mu_n - \mu_p = \mu_e = \mu_\mu. \quad (50)$$

The appearance of muons requires a sufficiently high chemical potential of electrons, i.e., $\mu_e > m_\mu$, where m_μ is the mass of muons. Equation (50) together with the charge neutral condition

$$\rho_p = \rho_e + \rho_\mu \quad (51)$$

determines the proton fraction x_p as a function of baryon density in the neutron star matter.

To calculate the core–crust transition density ρ_t , we only need to deal with the npe matter since muons will normally not appear as the electron chemical potential μ_e is not high enough near ρ_t unless one uses an extremely soft symmetry energy. For the npe matter at β -equilibrium, one has

$$\mu_n - \mu_p = \mu_e. \quad (52)$$

Then this identity, together with the charge neutral condition

$$\rho_p = \rho_e, \quad (53)$$

gives the corresponding x_p as a function of baryon density.

If analytical expressions of the EOS for asymmetric nuclear matter are known completely as given earlier for the Skyrme and MDI interactions, the exact β -equilibrium condition of Equation (24) can be used. However, often this is impossible with many interactions within various models. Instead, the parabolic approximation of the EOS is usually used. In this case, one has

$$\mu_e = \mu_\mu \approx 4(1 - 2x_p)E_{\text{sym}} = 4\delta E_{\text{sym}}. \quad (54)$$

Using both the full EOS and its parabolic approximation of the MDI interaction with $x = 0$ and $x = -1$, we have calculated the proton fraction x_p as a function of density from 0 to 1.6 fm^{-3} . The specific values of the parameter x chosen here are consistent with the constraints extracted from heavy-ion reactions (Li et al. 2008). The calculated values of x_p are shown in panel (c) of Figure 2. Compared to the results with $x = -1$, x_p with $x = 0$ is larger below the saturation density and smaller

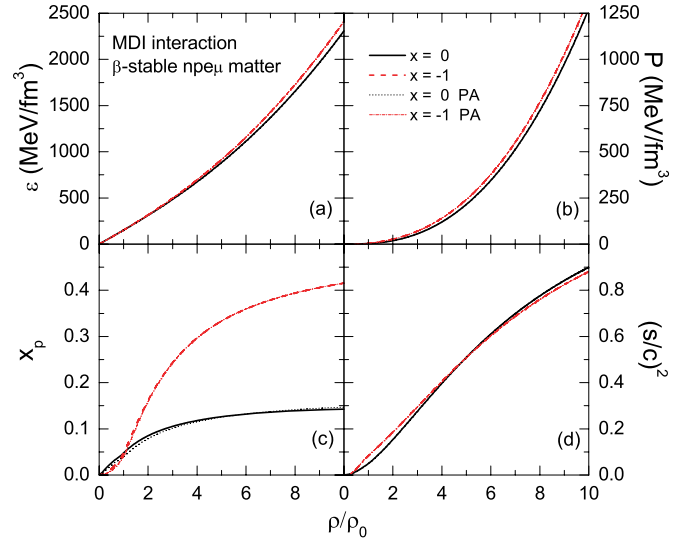


Figure 2. Density dependence of the energy density (a), the pressure (b), the proton fraction (c), and the sound velocity (d) for the MDI interaction with $x = 0$ and $x = -1$ for the $npe\mu$ matter at β -equilibrium. The results from the full EOS and its PA are compared.

(A color version of this figure is available in the online journal.)

at higher densities. The difference between calculations using the full EOS and its parabolic approximation is only visible at low densities for the soft symmetry energy with $x = 0$.

We now examine several thermodynamical quantities for the $npe\mu$ matter at β -equilibrium. The total energy density $\epsilon(\rho, \delta)$ consists of three parts: the baryon energy density $\epsilon_b(\rho, \delta)$, the electron energy density $\epsilon_e(\rho, \delta)$, and the muon energy density $\epsilon_\mu(\rho, \delta)$:

$$\epsilon(\rho, \delta) = \epsilon_b(\rho, \delta) + \epsilon_e(\rho, \delta) + \epsilon_\mu(\rho, \delta), \quad (55)$$

where

$$\epsilon_b(\rho, \delta) = \rho E_b(\rho, \delta) + \rho m, \quad (56)$$

with m being the baryon mass and ρ the total baryon density. The energy density of leptons $\epsilon_l(\rho, \delta)$ is calculated using the noninteracting Fermi gas model, and can be expressed as (Oppenheimer & Volkoff 1939)

$$\epsilon_l(\rho, \delta) = \eta \phi(t), \quad (57)$$

with

$$\eta = \frac{m_l c^2}{8\pi^2 \lambda^3},$$

and

$$\lambda = \frac{\hbar}{m_l c}, t = \lambda(3\pi^2 \rho_l)^{1/3},$$

$$\phi(t) = t\sqrt{1+t^2}(1+2t^2) - \ln(t + \sqrt{1+t^2}),$$

where m_l and ρ_l are the mass and number density of leptons.

Correspondingly, the total pressure $P(\rho, \delta)$ consists of the contributions from baryons, electrons, and muons, i.e.,

$$P(\rho, \delta) = P_b(\rho, \delta) + P_e(\rho, \delta) + P_\mu(\rho, \delta), \quad (58)$$

where

$$P_b(\rho, \delta) = \mu'_n \rho_n + \mu'_p \rho_p - \epsilon_b(\rho, \delta), \quad (59)$$

and here the chemical potentials should include the rest mass

$$\mu'_n = \mu_n + m, \mu'_p = \mu_p + m. \quad (60)$$

The pressure of leptons is written as

$$P_l(\rho, \delta) = \mu_l \rho_l - \epsilon_l(\rho, \delta), \quad (61)$$

where the chemical potential is

$$\mu_l = \sqrt{p_{fl}^2 + m_l^2}, \quad (62)$$

which is fully determined by the lepton density from

$$p_{fl} = \hbar(3\pi^2 \rho_l)^{1/3}. \quad (63)$$

Then, in this framework the thermodynamical consistency

$$P = \rho^2 \frac{d\epsilon/\rho}{d\rho} \quad (64)$$

is satisfied.

The exact expressions given above can be carried out using the full EOS. In some cases, the parabolic approximation is used. Instead of Equations (56) and (59), within the parabolic approximation one has

$$\epsilon_b(\rho, \delta) = \rho[E_0(\rho) + E_{\text{sym}}(\rho)\delta^2] + \rho m, \quad (65)$$

$$P_b(\rho, \delta) = \rho^2(E'_0(\rho) + E'_{\text{sym}}(\rho)\delta^2). \quad (66)$$

This approximation still satisfy the thermodynamical consistency (Equation (64)).

The density dependence of the total energy density and pressure is shown in panels (a) and (b) of Figure 2, respectively. The difference between calculations using the full EOS and its PA is essentially invisible. The stiffer (e.g., $x = -1$) the symmetry energy is, the larger the total energy and pressure are, as one expects.

The causality requires that the sound speed s in nuclear matter remains smaller than the speed of light in vacuum c , i.e.,

$$\frac{s}{c} = \sqrt{\frac{\partial P}{\partial \epsilon}} < 1. \quad (67)$$

In panel (d) of Figure 2 we examine the speed of sound for the MDI interaction with $x = 0$ and $x = -1$. It is seen that the causality is satisfied in the whole density range considered.

4. KEY EQUATIONS FOR DESCRIBING THE STRUCTURE OF NEUTRON STARS

For completeness, we quote here from the general literature (see, e.g., Morrison et al. 2004) some key equations to be used later in our studies of the neutron star structure. For slowly rotating neutron stars where spherical symmetry is conserved approximately, the moment of inertia is

$$I = \left(\frac{\partial J}{\partial \Omega} \right)_{\Omega=0} = \frac{J}{\Omega}, \quad (68)$$

where Ω is the angular velocity measured in a far-away inertial system, and J is the angular momentum. In the slow-rotation

limit in spherical polar coordinates, the metric can be written as ($G = c = 1$):

$$(ds)^2 = -e^\nu(dt)^2 + \left(1 - \frac{2m_g}{r}\right)^{-1} (dr)^2 - 2\omega r^2 \sin^2 \theta dt d\phi + r^2(d\theta^2 + \sin^2 \theta d\phi^2), \quad (69)$$

where $\omega(r) \equiv \frac{d\phi}{dt}$ is the angular velocity of the local slow-rotation system (measured in a far-away inertial system), and $m_g(r)$ is the neutron star gravitational mass inside a radius r :

$$\frac{dm_g(r)}{dr} = 4\pi r^2 \epsilon(r), \quad (70)$$

with $\epsilon(r)$ being the energy density. Defining

$$\bar{\omega} = \Omega - \omega, \quad (71)$$

then from the metric of the geometry outside a slow-rotation star, one can get

$$r^{-4} \frac{d}{dr} \left[r^4 j(r) \frac{d\bar{\omega}}{dr} \right] + 4r^{-1} \frac{dj}{dr} \bar{\omega}(r) = 0, \quad (72)$$

where

$$j(r) = \exp \left[-\frac{1}{2}(\lambda(r) + \nu(r)) \right], \quad (73)$$

with

$$e^{\lambda(r)} = \left(1 - \frac{2m_g}{r}\right)^{-1}, \quad (74)$$

and

$$\frac{d\nu}{dr} = -\frac{2}{\epsilon + P} \frac{dP}{dr}. \quad (75)$$

The pressure, $P(r)$, is obtained from the famous Tolman–Oppenheimer–Volkoff (TOV) equation, i.e.,

$$\frac{dP}{dr} = -(\epsilon + P) \frac{m_g + 4\pi r^3 P}{r(r - 2m_g)}. \quad (76)$$

For convenience, an additional function $\eta(r)$ can be defined as

$$\eta(r) = \frac{d\bar{\omega}}{dr}, \quad (77)$$

and the boundary conditions at the center of the star are

$$\bar{\omega}(0) = \text{constant}, \quad (78)$$

and the constant is chosen so that

$$\eta(0) = 0. \quad (79)$$

Outside the star we should have

$$e^\nu = 1 - \frac{2M}{r} \quad (80)$$

and

$$\omega = \frac{2J}{r^3}, \quad (81)$$

where

$$J = \frac{1}{6} R^4 \eta(R) \quad (82)$$

and M and R are the total gravitational mass and the total radius of the neutron star, respectively. To make the variables continuous at the surface of the star, we have the boundary conditions

$$\bar{\omega}(R) = \Omega - \eta(R)\frac{R}{3}, \quad v(R) = \ln(1 - 2M/R). \quad (83)$$

In this framework, after solving the differential Equations (70), (72), (75), and (76), the mass, radius, and moment of inertia can be calculated. Following the standard procedure, we integrate out the TOV and other differential equations starting from the center to the surface where the pressure vanishes, i.e., $P(R) = 0$. The latter defines the total radius R of the neutron star. Then the total gravitational mass of the neutron star is obtained from integrating Equation (70) as

$$M \equiv m_g(R) = 4\pi \int_0^R dr r^2 \epsilon(r). \quad (84)$$

The total moment of inertia of the neutron star is obtained similarly. By integrating only to the transition density ρ_t , one can obtain the radius and mass of the core. The thickness, mass, and moment of inertia of the crust can be obtained from taking the differences between values for the whole and the core of neutron stars.

5. RESULTS AND DISCUSSION

In the following, we present and discuss the results of our calculations on the transition density and pressure at the inner edge and several global properties of neutron stars. Applying formalisms outlined in the previous sections, we illustrate numerically and discuss several issues including (1) relationships among the mechanical, chemical, and total instability boundaries in asymmetric nuclear matter, and their relevance for locating the core–crust transition density in the npe matter at β -equilibrium; (2) the difference between the core–crust transition densities obtained using the dynamical and thermodynamical methods using the same interactions; (3) understanding the difference between the core–crust transition densities obtained with the full EOS and its parabolic approximation using the same methods and interactions; (4) the systematics of the transition density by varying the stiffness of the symmetry energy; (5) limits on the transition density using the symmetry energy constrained by heavy-ion experiments; (6) relationship between the transition density and the size of the neutron skin in ^{208}Pb ; (7) systematics and constraints on the transition pressure at the core–crust boundary. We will then study several global properties of neutron stars including the mass, radius, and the moment of inertia as well as their crustal fractions. The focus will be on effects of the density dependence of the symmetry energy on these observables. We will also check the inner crust EOS dependence of properties of neutron stars.

5.1. Instabilities in Neutron-Rich Matter and the Core–Crust Transition Density in Neutron Stars at β -Equilibrium

In Section 2.3, we studied analytically the relationship between the dynamical and thermodynamical methods. To appreciate the relationship more clearly and quantitatively, we present here a numerical example in the ρ_p versus ρ_n plane. First, it is important to recognize that the right-hand side of Equation (32) just determines the thermodynamical instability of asymmetric nuclear matter. Shown in Figure 3 are the boundaries of the

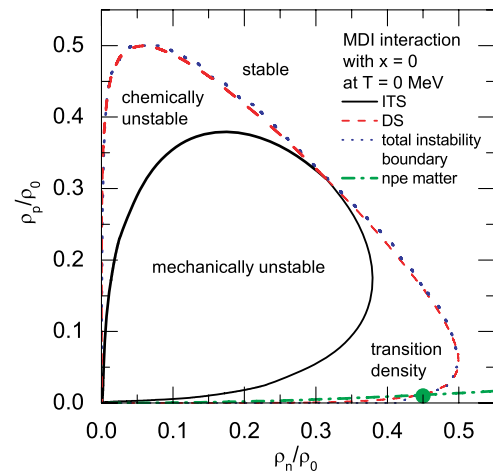


Figure 3. Mechanical, chemical, and total instability boundaries shown in the $\rho_n \sim \rho_p$ plane using the MDI interaction with $x = 0$ at zero temperature. ρ_n vs. ρ_p for the npe matter at β -equilibrium is shown as the dash-dot line. The core–crust transition density from the thermodynamical method is indicated with the filled dot.

(A color version of this figure is available in the online journal.)

mechanical (also known as the isothermal spinodal or ITS), chemical (also known as the diffusive spinodal or DS), and total instabilities without requiring β -equilibrium and charge neutrality using the MDI interaction with $x = 0$ at zero temperature. A similar figure has been shown in our previous paper (Xu et al. 2008) but in the $\rho \sim \delta$ or $P \sim \rho$ plane at finite temperatures. Inside the ITS curve, the system is mechanically unstable, while between the ITS and DS curves the system is chemically unstable. The total instability is identified by the condition

$$\frac{\partial \mu_n}{\partial \rho_n} \frac{\partial \mu_p}{\partial \rho_p} - \left(\frac{\partial \mu_n}{\partial \rho_p} \right)^2 < 0. \quad (85)$$

It is seen clearly that the total instability region obtained using the above condition covers the region of both mechanical and chemical instabilities. This observation is consistent with the earlier finding by Margueron and Chomaz (2003). In the npe matter when the β -equilibrium and charge neutrality conditions are imposed, the ρ_n and ρ_p are correlated with each other. For the MDI interaction, this correlation can be obtained from the x_p versus ρ curves shown in panel (c) of Figure 2. With $x = 0$, this correlation is shown with the dash-dot line in Figure 3. The cross point of this line and the boundary of total instability corresponds to the core–crust transition density in the npe matter within the thermodynamical approach. The density gradient term and the Coulomb interaction generally reduce slightly the instability region; thus the dynamical method normally leads to a slightly lower transition density.

It is necessary to note here that the onset of instabilities has been associated with the so-called liquid–gas phase transition in nuclear matter (Siemens 1983). An experimental manifestation of the liquid–gas phase transition is the well known multifragmentation phenomenon in heavy-ion collisions (see, e.g., Chomaz et al. 2004; Das et al. 2005 for a recent review). It is seen from Figure 3 that both the dynamical and thermodynamical models give a liquid–gas phase transition density of about $0.63\rho_0$ for symmetric (i.e., $\rho_n = \rho_p$) nuclear matter (SNM) at $T = 0$. While the latter depends slightly on the interaction used, it is consistent with previous calculations on the boundary of mechanical instability in cold SNM (see, e.g., Müller & Serot

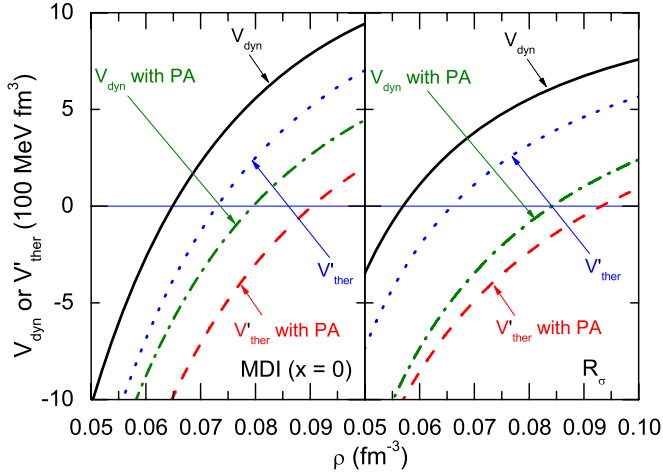


Figure 4. Density dependence of V for the MDI interaction with $x = 0$ (left panel) and the Skyrme force R_σ (right panel) using both the dynamical and thermodynamical methods with the full EOS and its PA.

(A color version of this figure is available in the online journal.)

1995; Li & Ko 1997). We thus conclude that both the dynamical and thermodynamical methods give the right asymptotical value for the transition density when one goes from the npe matter to symmetric nuclear matter at $T = 0$.

5.2. Constraining the Core–Crust Transition Density in Neutron Stars

We now turn to the numerical calculations and comparisons of the core–crust transition densities within both the dynamical and thermodynamical methods using the full EOS and its PA with the MDI and Skyrme interactions. The transition density can be obtained directly by carrying out the analyses in the ρ versus x_p plane. We stress again that, in principle, the transition density should be calculated from Equation (12) or Equation (21), and the β -equilibrium condition should be expressed as Equation (24). In practical calculations the parabolic approximation has often been used in determining the β -equilibrium condition using Equation (54) and in evaluating V_{ther} using Equation (23). To first evaluate effects of the PA, we show in Figure 4 the density dependence of V_{dyn} and V'_{ther} using the MDI interaction with $x = 0$ and the Skyrme force R_σ within both the dynamical and thermodynamical methods with the full EOS and its PA. Here, we have defined

$$V'_{\text{ther}} = V_{\text{ther}} \frac{\partial^2 E_b}{\partial x_p^2} / \left(\rho^2 \frac{\partial \mu_n}{\partial \rho_n} \right), \quad (86)$$

and it should be noted that V'_{ther} has the same vanishing point as V_{ther} and the same dimension as V_{dyn} . For the MDI interaction with $x = 0$, the transition densities using the full EOS within the dynamical and thermodynamical methods are 0.065 fm^{-3} and 0.073 fm^{-3} , respectively, while the corresponding results using the PA are 0.080 fm^{-3} and 0.090 fm^{-3} , respectively. For the Skyrme force R_σ , the transition densities are 0.057 fm^{-3} and 0.066 fm^{-3} using the full EOS, while the corresponding values with the PA are 0.084 fm^{-3} and 0.093 fm^{-3} , using the dynamical and thermodynamical methods, respectively. Thus, the transition densities are generally lower with the dynamical method as we mentioned earlier, as the density gradient term and the Coulomb interaction make the system more stable. However, the PA significantly lifts the transition density regardless of the

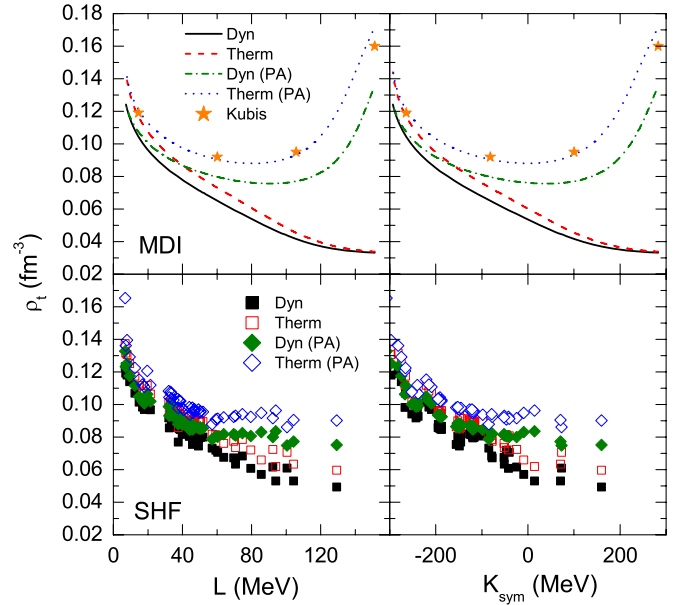


Figure 5. Transition density as a function of L (left panel) and K_{sym} (right panel) using both the dynamical and thermodynamical methods with the full EOS and its parabolic approximation. The MDI (upper panels) and Skyrme interactions (lower panels) are used.

(A color version of this figure is available in the online journal.)

approach used. In fact, the difference between calculations using the full EOS and its PA is much larger than that caused by using the two different methods.

As we have mentioned in the Introduction, it is well known that the transition density depends sensitively on $E_{\text{sym}}(\rho)$. Many interesting studies (see, e.g., Oyamatsu & Iida 2007; Lattimer & Prakash 2007; Douchin & Haensel 2000) have been carried out using various $E_{\text{sym}}(\rho)$. In the following, we present and compare the systematics of the transition density using the MDI interaction with varying parameter x and 51 Skyrme forces. Since the density dependence of the symmetry energy can be well characterized by the parameters L and K_{sym} , we examine ρ_t as a function of L and K_{sym} in Figure 5. Shown in the left panels are ρ_t as a function of L using both the dynamical and thermodynamical methods with the full EOS and its PA. The same quantities are shown as a function of K_{sym} in the right panels. It is interesting to see that both the dynamical and thermodynamical methods give very similar results, with the former giving slightly smaller ρ_t than the latter (the difference is actually less than 0.01 fm^{-3}), and this is due to the fact that the former includes the density gradient and Coulomb terms which make the system more stable and lower the transition density. The small difference between the two methods implies that the effects of density gradient and Coulomb terms are unimportant in determining ρ_t . In addition, it is also interesting to see that the transition density decreases almost linearly with increasing L , especially in the calculations with the full EOS. This observation is consistent with that found recently by Oyamatsu et al. (Oyamatsu & Iida 2007). We note here that there are some interactions with larger x values in the MDI interaction, giving negative and/or very small values for the parameter L . These interactions with negative and/or very small values for the parameter L , however, lead to neutron skins in ^{208}Pb inconsistent with the existing data (Steiner & Li 2005b; Chen et al. 2005b). Since they are still somewhat theoretically interesting, we have thus also examined the possible transition density with these

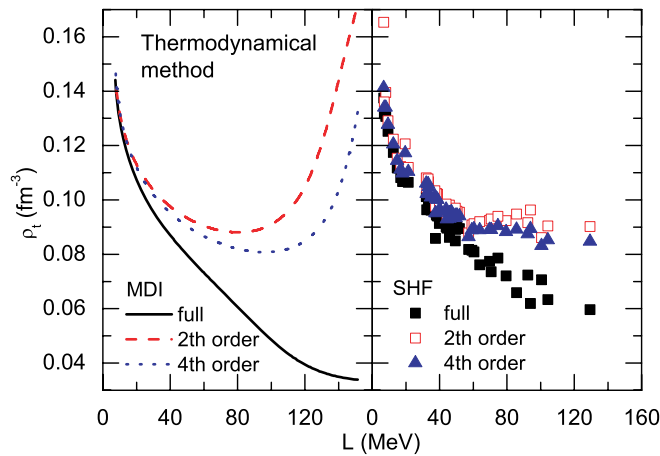


Figure 6. Relation between the transition density and L using the thermodynamical method with the MDI (left panel) and Skyrme (right panel) interactions. For both kinds of interactions, up to the second and fourth orders in isospin asymmetry are used in the expansions of the corresponding full EOS.

(A color version of this figure is available in the online journal.)

interactions. We find that for interaction parameters with $L < 7$ MeV in the MDI interaction ($x > 1.17$), the transition density does not exist and the npe matter is always unstable. This is due to the fact that the symmetry energy is so soft that $\frac{\partial \mu_n}{\partial \rho_n}$ is always negative, while $\frac{\partial \mu_p}{\partial \rho_p}$ is always positive at low densities, and thus the stability condition $\frac{\partial \mu_n}{\partial \rho_n} \frac{\partial \mu_p}{\partial \rho_p} - \left(\frac{\partial \mu_n}{\partial \rho_p} \right)^2 > 0$ can never be satisfied.

It is clear from all existing calculations that ρ_t is sensitive to the density dependence of the nuclear symmetry energy. The latter can be well characterized by the slope L and the curvature K_{sym} . Naturally, there are some correlations between L and K_{sym} determined by the interaction energy density functional used. For the MDI interaction, L and K_{sym} both change linearly with the parameter x . Therefore they are linearly correlated. Similarly, L and K_{sym} are also correlated within the SHF model. It is therefore not surprising that the variation of ρ_t with K_{sym} is very similar to that with L , as shown in the right panels of Figure 5.

We now apply the experimentally constrained L to the ρ_t - L correlation obtained using the full EOS within the dynamical method in constraining ρ_t . In our earlier transport model studies of the isospin diffusion data in heavy-ion reactions (Chen et al. 2005a; Li & Chen 2005), the complete MDI interaction was used. The extracted L value is 88 ± 25 MeV if one defines E_{sym} using the PA in Equation (35) or 86 ± 25 MeV if one uses the exact expression of E_{sym} (Equation (49)) corresponding to the full MDI EOS. Using the latter in comparison with the full MDI results shown in Figure 6, we conclude that the transition density is between 0.040 fm^{-3} and 0.065 fm^{-3} . This constrained range is significantly below the fiducial value of $\rho_t \approx 0.08 \text{ fm}^{-3}$ often used in the literature and the estimate of $0.5 < \rho_t/\rho_0 < 0.7$ made in Lattimer & Prakash (2007) within the thermodynamical approach using the parabolic approximation of the EOS. This difference is understandable, as we shall explain in detail below.

5.3. Understanding Effects of the Parabolic Approximation of the EOS on the Core-Crust Transition Density in Neutron Stars

It is also seen from Figure 5 that, except at very small values of L and K_{sym} , there is a big difference between results obtained using the full EOS and its parabolic approximation within both

the dynamical and thermodynamical methods. Especially at high values of L and K_{sym} , the ρ_t from the PA increases, while the one from the full EOS continuously decreases. We also note that Kubis's calculations (Kubis 2004, 2007) coincide with our results using the MDI interaction within the thermodynamical method with the PA. Why is the transition density so sensitive to whether one uses the PA or not? To answer this question, we first note that both the first and second derivatives of the EOS are involved in the stability conditions. The EOS can be expanded according to $E_b(\rho, x_p)$ up to the fourth-order term of $(1 - 2x_p)$ according to

$$E_b(\rho, x_p) = E_0(\rho) + E_{\text{sym}}(\rho)(1 - 2x_p)^2 + E_4(\rho)(1 - 2x_p)^4 + O(1 - 2x_p)^6. \quad (87)$$

Only even-order terms of $(1 - 2x_p)$ appear as the strong interaction is assumed to be symmetric for exchanging neutrons with protons. The first- and second-order derivatives of the energy with respect to x_p are, respectively,

$$\frac{\partial E_b}{\partial x_p} = -4E_{\text{sym}}(\rho)(1 - 2x_p) - 8E_4(\rho)(1 - 2x_p)^3 + O(1 - 2x_p)^5. \quad (88)$$

$$\frac{\partial^2 E_b}{\partial x_p^2} = 8E_{\text{sym}}(\rho) + 48E_4(\rho)(1 - 2x_p)^2 + O(1 - 2x_p)^4. \quad (89)$$

At β -equilibrium, the npe matter is usually highly neutron rich, so $(1 - 2x_p)$ is not far from 1. Thus the higher-order terms in $(1 - 2x_p)$ are normally not negligible. Moreover, although the coefficient E_4 is normally smaller than E_{sym} , the contributions to $\frac{\partial E_b}{\partial x_p}$ and $\frac{\partial^2 E_b}{\partial x_p^2}$ from the E_4 term gain a factor of 2 and 6, respectively, compared to that from the E_{sym} term. Thus, mathematically one expects the E_4 term to play an important role in locating the stability boundaries in asymmetric nuclear matter and the core-crust transition density in neutron stars. It is also easy to understand why the effect is stronger with stiffer symmetry energy functionals. At subsaturation densities near ρ_t , the proton fraction x_p is lower with the stiffer symmetry energy. It is the opposite at suprasaturation densities. A numerical example can be found in panel (c) of Figure 2 for the MDI interaction with $x = 0$ (softer) and $x = -1$ (stiffer). It is seen that with the stiffer symmetry of $x = -1$, near the transition density $(1 - 2x_p)$ is indeed larger than that with a softer symmetry energy of $x = 0$. Therefore, a larger error will be introduced in calculating ρ_t using the parabolic approximation with stiffer symmetry energy functionals. To be more quantitative, we compare in Figure 6 ρ_t as a function of L obtained within the thermodynamical method using the full EOS with ρ_t obtained by expanding the EOS to the second and fourth orders in $(1 - 2x_p)$. The left panel is for calculations with the MDI interaction, and the right one with the 51 Skyrme forces. We note that the convergence speed is very slow, and not only the fourth-order term but also the sixth-, eighth-, or even further higher-order terms should be considered. (For the Skyrme forces, we noted that the calculations up to the eighth-order approximation still lead to a significant error compared to the full EOS.) We also note here that the EOS of asymmetric nuclear matter always contains higher-order terms in isospin asymmetry at least due to the kinetic contribution. Moreover, if we use Equation (35) instead of Equation (36) in calculating the symmetry energy and then reconstruct the EOS as $E(\rho, \delta) = E(\rho, \delta = 0) + [E(\rho, \delta = 1)$

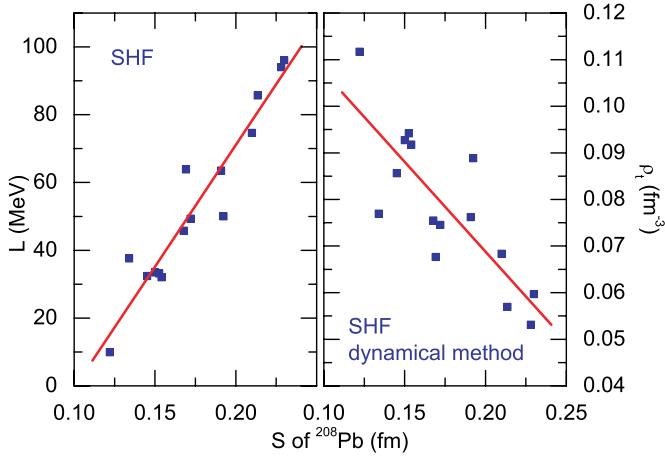


Figure 7. Slope parameter L and the transition density ρ_t as a function of the neutron skin thickness S of ^{208}Pb using the dynamical method with the full EOS with the Skyrme interactions. The solid lines indicate the linear fits.

(A color version of this figure is available in the online journal.)

$-E(\rho, \delta = 0)]\delta^2 + O(\delta^4)$ as in the parabolic approximation, almost the same transition densities are obtained as the second-order approximation shown in Figure 6. Our results thus indicate that one may introduce a huge error by assuming a priori that the EOS is parabolic for a given interaction in calculating ρ_t . It is thus clear that the correct transition density can hardly be obtained without knowing the exact expression of $E_b(\rho, x_p)$ for a given interaction. Interestingly, these features agree with the early finding (Arponen 1972) that ρ_t is very sensitive to the fine details of the nuclear EOS.

5.4. Correlation between the Core–Crust Transition Density in Neutron Stars and the Size of the Neutron Skin in ^{208}Pb

It is also well known that the sizes of neutron skins in heavy nuclei are sensitive to the symmetry energy at subsaturation densities see, e.g., (Brown 2000; Horowitz & Piekarewicz 2001; Furnstahl 2002; Dieperink et al. 2003; Steiner et al. 2005a; Todd-Rutel & Piekarewicz 2005; Chen et al. 2005b). However, available data on neutron skin thickness obtained using hadronic probes are not accurate enough yet to constrain tightly the symmetry energy. Interestingly, the parity radius experiment (PREX) at the Jefferson Laboratory aiming to measure the neutron radius of ^{208}Pb via parity violating electron scattering (Jefferson Laboratory Experiment E-00-003; Horowitz et al. 2001) hopefully will provide much more precise data in the near future. It can then potentially constrain the symmetry energy at low densities and thus the core–crust transition density more stringently. It has been shown by many authors and also in our previous work (Chen et al. 2005b) that the neutron skin thickness S increases linearly with L . Given the fact that the transition density ρ_t decreases almost linearly with increasing L as shown above, it is interesting to examine the correlation between S and ρ_t . Such a study was first carried out by Horowitz & Piekarewicz (2001) using the RMF EOS and ρ_t calculated within the RPA approach.

Shown in Figure 7 are ρ_t and L versus the neutron skin thickness S of ^{208}Pb obtained using the dynamical method with the full SHF EOS. As known before, the neutron skin thickness increases linearly with increasing L (Chen et al. 2005b). Moreover, the transition density shows a decreasing trend with increasing neutron skin thickness. As the ρ_0 and $E_{\text{sym}}(\rho_0)$ are different for the various sets of Skyrme forces,

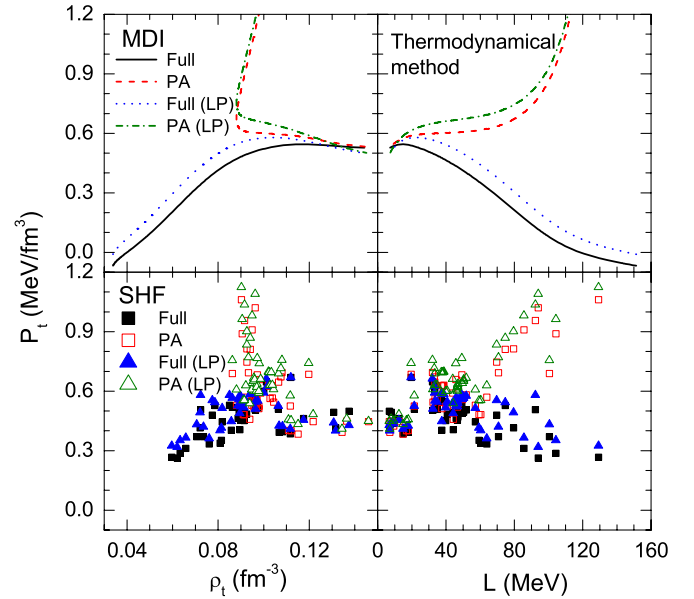


Figure 8. Transition pressure P_t as a function of ρ_t and L within the thermodynamical method with the full EOS and its parabolic approximation using the MDI (upper panels) and Skyrme (lower panels) interactions.

(A color version of this figure is available in the online journal.)

the data points do not show a very strong linear correlation. However, the tendency is clear. This trend is consistent with the RPA calculations using the RMF EOSs by Horowitz et al. (Horowitz & Piekarewicz 2001; Carriere et al. 2003).

5.5. The Pressure at the Inner Edge of the Neutron Star Crust

The pressure at the inner edge is an important quantity related directly with the crustal fraction of the moment of inertia which can be measured indirectly from observations of pulsar glitches (Lattimer & Prakash 2007). In principle, having determined the transition density it is straightforward to calculate the corresponding pressure using the formalisms outlined in Section 3.3. Before presenting the numerical results, it is very instructive to quote the analytical estimation obtained by Lattimer and Prakash (2007) for the transition pressure,

$$P_t = \frac{K_0 \rho_t^2}{9 \rho_0} \left(\frac{\rho_t}{\rho_0} - 1 \right) + \rho_t \delta_t \left[\frac{1 - \delta_t}{2} E_{\text{sym}}(\rho_t) + \left(\rho \frac{dE_{\text{sym}}(\rho)}{d\rho} \right)_{\rho_t} \delta_t \right], \quad (90)$$

where K_0 is the incompressibility of SNM at ρ_0 , and δ_t is the isospin asymmetry at ρ_t . Besides the implicit dependence on the symmetry energy through ρ_t and δ_t , P_t also depends explicitly on the value and slope of $E_{\text{sym}}(\rho)$ at ρ_t . Thus P_t depends very sensitively on $E_{\text{sym}}(\rho)$. Noticing that Equation (90) is an estimate using the thermodynamical method with the PA, it is interesting to compare numerically its predictions with the results obtained according to the original formalisms in Section 3.3 using both the full EOS and its PA within the thermodynamical and dynamical method separately.

In Figure 8, we show P_t as a function of ρ_t (left panels) and L (right panels) using the thermodynamical method with and without the parabolic approximation. The same quantities with the dynamical method are shown in Figure 9. Both the MDI (upper panels) and Skyrme (lower panels) interactions

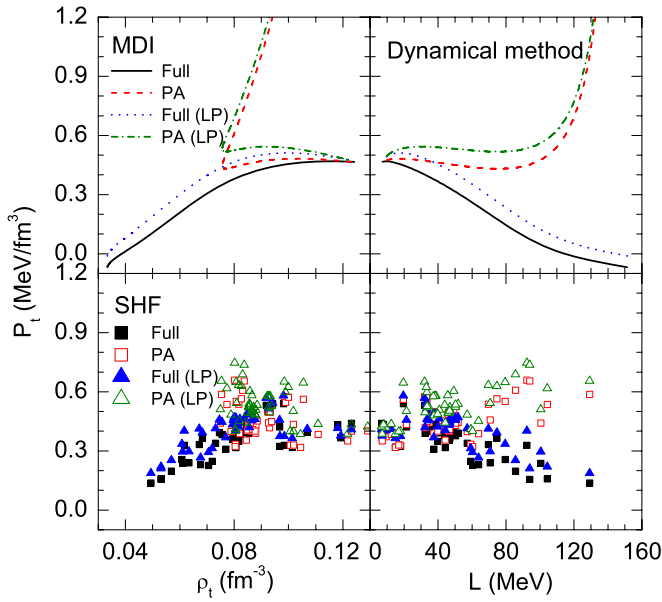


Figure 9. Same as Figure 8, but within the dynamical method. (A color version of this figure is available in the online journal.)

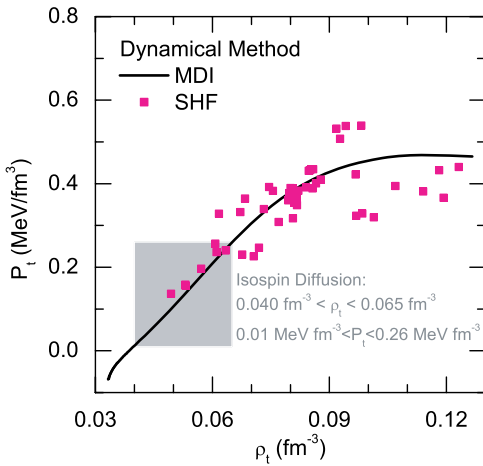


Figure 10. P_t as a function of ρ_t using the dynamical method without parabolic approximation for both the MDI interaction and SHF calculations. The shaded band represents the constraint from the isospin diffusion data. (A color version of this figure is available in the online journal.)

are used. The results from Equation (90) using the ρ_t and E_{sym} corresponding to the full EOS and its PA are also shown for comparison. It is interesting to see that Equation (90) predicts qualitatively the same but quantitatively slightly higher values compared to the original expressions for the pressure with or without the PA for both the thermodynamical and dynamical methods even though this formula was derived from the thermodynamical method using the PA. This observation is consistent with the results shown in panel (b) of Figure 2, namely the direct effect of using the full EOS or its PA on the pressure is small although the PA may affect strongly the transition pressure P_t by changing the transition density ρ_t . P_t essentially increases with increasing ρ_t in calculations using the full EOS, but a complex relation between P_t and ρ_t is obtained using the PA. The observed large difference in P_t is due to the strong PA effect on the ρ_t . Moreover, the latter does not vary monotonically with L for the PA as shown in Figure 5.

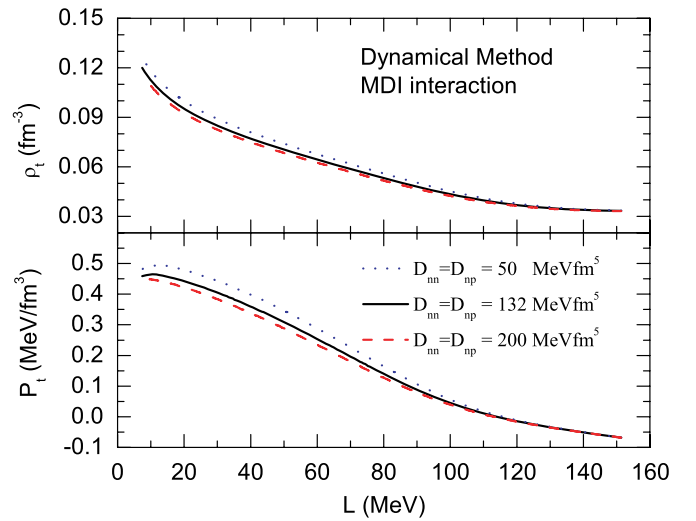


Figure 11. ρ_t and P_t as a function of L using the dynamical method for the MDI interaction with different values of $D_{pp} = D_{nn} = D_{np} = D_{pn}$. (A color version of this figure is available in the online journal.)

Thus the PA of the EOS leads to a very different P_t compared to the calculations with the full EOS especially for the stiffer symmetry energy functionals.

It is also interesting to examine the range of P_t corresponding to the ρ_t and L constrained by the heavy-ion reaction data. In Figure 10, we show P_t as a function of ρ_t using the dynamical method and the full EOS for both the MDI (solid line) and the Skyrme (filled squares) calculations. It is interesting to see that the MDI and Skyrme interactions give generally quite consistent results. Corresponding to ρ_t constrained in between 0.040 fm^{-3} and 0.065 fm^{-3} , P_t is limited between 0.01 MeV fm^{-3} and 0.26 MeV fm^{-3} with the MDI interaction as indicated by the shaded area, which is significantly less than the fiducial value of $P_t \approx 0.65 \text{ MeV fm}^{-3}$ often used in the literature (Lattimer & Prakash 2007). As pointed out in a recent work by Avancini et al (2009), the value of $P_t \approx 0.65 \text{ MeV fm}^{-3}$ may be too large for most mean-field calculations without the PA. We notice here that among the 51 Skyrme interactions listed in Table 1, the following seven interactions, i.e., SkMP, SKO, R_σ , G_σ , SkI2, SkI3, and SkI5, are consistent with the constraints from heavy-ion reactions.

In closing this subsection, we examine how the transition density and pressure may be sensitive to variations of the coefficients $D_{pp} = D_{nn} = D_{np}$ in the MDI interaction. As we have pointed out in Section 2.1 for the dynamical method, we introduced phenomenologically the empirical values of $D_{pp} = D_{nn} = D_{np} = 132 \text{ MeV fm}^5$ for the gradient coefficients in the MDI interaction. These values are obviously not obtained self-consistently. Shown in Figure 11 are ρ_t and P_t as functions of L using the dynamical method with the full MDI EOS but different values of the coefficients $D_{pp} = D_{nn} = D_{np}$, namely $D_{pp} = D_{nn} = D_{np} = 50, 132,$ and 200 MeV fm^5 , respectively. We note from Figure 11 that changing the value of $D_{pp} = D_{nn} = D_{np}$ from 50 to 200 MeV fm^5 leads to at most a variation of about 0.007 fm^{-3} for ρ_t and 0.06 MeV fm^{-3} for P_t . These results thus indicate that the transition density and pressure are rather insensitive to the variation of $D_{pp} = D_{nn}$ and $D_{np} = D_{pn}$.

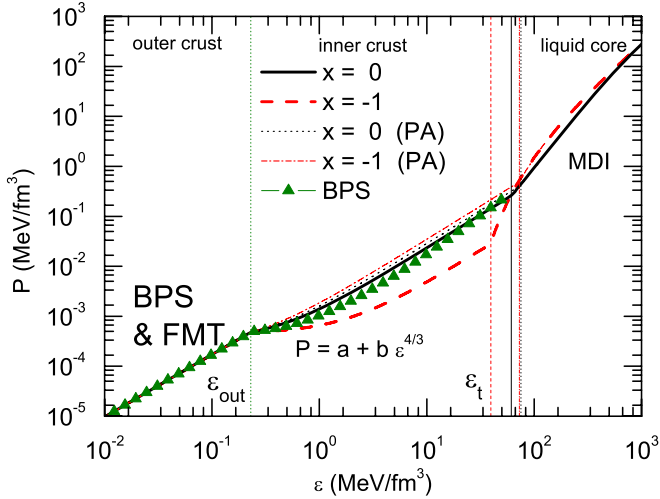


Figure 12. EOS of different parts of neutron stars. The energy density at ρ_t and ρ_{out} is indicated as ϵ_t and ϵ_{out} , respectively, and the full and PA results of the MDI interaction with $x = 0$ and $x = -1$ are shown.

(A color version of this figure is available in the online journal.)

5.6. Constructing the EOS from the Center to the Surface of Neutron Stars

With a clear understanding about the core–crust transition density as we discussed above, we now investigate several other properties of the crust and the whole neutron star. To proceed, it is necessary to know the EOS over a broad density range from the center to the surface of neutron stars. Besides the possible appearance of nuclear pasta in the crust, various phase transitions and non-nucleonic degrees of freedom may appear in the core. In this work, we restrict ourselves to the simplest and traditional model. We make the minimum assumption that the core contains the uniform $npe\mu$ matter only, and there is no phase transition. Results from this kind of calculation serve as a useful baseline for understanding general features of astrophysical observations. Significant deviations from observations may indicate the onset of nontraditional physics.

For the core, we use the MDI EOS and its PA shown in Figure 2. In the inner crust of densities between ρ_{out} and ρ_t where the nuclear pastas may exist, because of our poor knowledge about its EOS from first principles, following Carriere et al. (2003), we construct its EOS according to

$$P = a + b\epsilon^{4/3}. \quad (91)$$

This polytropic form with an index of $4/3$ has been found to be a good approximation to the crust EOS (Link et al. 1999; Lattimer & Prakash 2000, 2001), and we will discuss how our results are sensitive to the polytropic index later. $\rho_{\text{out}} = 2.46 \times 10^{-13} \text{ fm}^{-3}$ is the density separating the inner from the outer crust. The constants a and b are determined by

$$a = \frac{P_{\text{out}}\epsilon_t^{4/3} - P_t\epsilon_{\text{out}}^{4/3}}{\epsilon_t^{4/3} - \epsilon_{\text{out}}^{4/3}}, \quad b = \frac{P_t - P_{\text{out}}}{\epsilon_t^{4/3} - \epsilon_{\text{out}}^{4/3}}, \quad (92)$$

where P_t , ϵ_t and P_{out} , ϵ_{out} are the pressure and energy density at ρ_t and ρ_{out} , respectively. In the outer crust with $6.93 \times 10^{-13} \text{ fm}^{-3} < \rho < \rho_{\text{out}}$, we use the EOS of BPS (Baym et al.

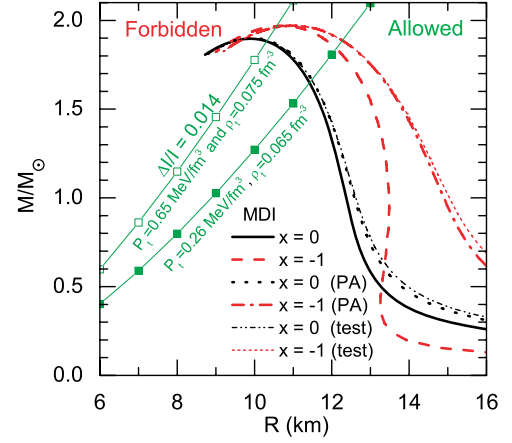


Figure 13. M – R relation of static neutron stars from the full EOS and its parabolic approximation as well as the test case (see the text for details) with the MDI interaction with $x = 0$ and $x = -1$. For the Vela pulsar, the constraint $\Delta I/I > 0.014$ implies that allowed masses and radii lie to the right of the line linked with solid squares ($\rho_t = 0.065 \text{ fm}^{-3}$ and $P_t = 0.26 \text{ MeV fm}^{-3}$, obtained in the present work) or open squares ($\rho_t = 0.075 \text{ fm}^{-3}$ and $P_t = 0.65 \text{ MeV fm}^{-3}$, used in Link et al. 1999).

(A color version of this figure is available in the online journal.)

1971a; Iida & Sato 1997), and in the region of $4.73 \times 10^{-15} \text{ fm}^{-3} < \rho < 6.93 \times 10^{-13} \text{ fm}^{-3}$ we use the EOS of FMT (Baym et al. 1971a).

Shown in Figure 12 are the selected EOSs for the different parts of the neutron star. As we have discussed earlier, ρ_t is obtained by studying the onset of instabilities in the core, namely it is the critical density below which small density fluctuations will grow exponentially. ρ_t is thus determined by the EOS of the core only. We use here the ρ_t obtained within the dynamical method using the full EOS and its parabolic approximation with the MDI interaction and $x = 0$ and $x = -1$. The corresponding values of ϵ_t are indicated by the vertical lines in Figure 12. Using the above combination of EOSs for the different parts of the neutron star, the radial distribution of the total energy density and the pressure in neutron stars is continuous as required, but the derivative of the pressure is not continuous at ρ_t and ρ_{out} . It is seen that the EOS for the inner crust is quite different using the full EOS or its PA especially with $x = -1$. Interestingly, one can see that the famous BPS EOS extended to the inner crust is between the parameterized EOSs with $x = 0$ and $x = -1$.

5.7. The Mass–Radius Correlation of Neutron Stars

With the EOS constructed above, in the next three subsections we study several key properties of the crust and the whole neutron star using the formalisms outline in Section 4. We carry out numerical calculations for all quantities of interest. For the crustal fraction of the moment of inertia, we also compare our numerical calculations with predictions of the analytical expression put forward by Lattimer and Prakash (2000, 2001, 2007). In this subsection, we focus on effects of the symmetry energy on the mass–radius correlation. We use the MDI interaction with $x = 0$ and $x = -1$ consistent with the existing heavy-ion reaction data (Li et al. 2008).

The resulting mass–radius correlation is shown in Figure 13. For the softer symmetry energy ($x = 0$) M decreases with increasing R , while for the stiffer symmetry energy ($x = -1$) the radius remains almost unchanged or even decreases with decreasing mass near $R = 13.5 \text{ km}$. For $M > 0.53 M_{\odot}$, the radius is larger for $x = -1$, while for $M < 0.53 M_{\odot}$ the radius

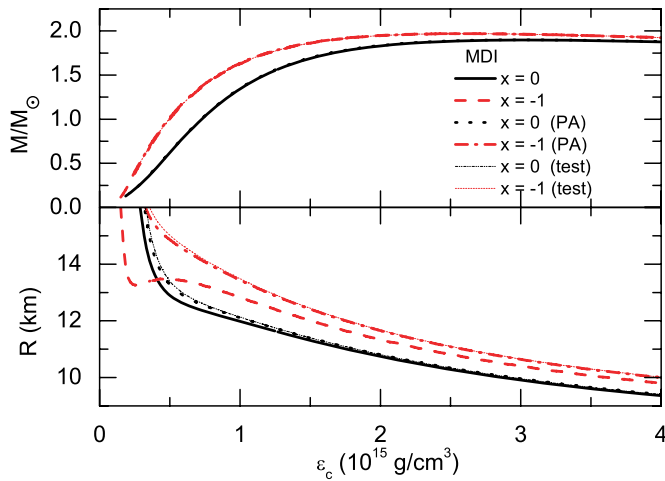


Figure 14. Mass and radius of neutron stars as functions of the central energy density using the MDI interaction with $x = 0$ and $x = -1$. The results from three methods are shown for comparison. See the text for details.

(A color version of this figure is available in the online journal.)

is larger for $x = 0$. For nucleonic matter, a stiffer symmetry energy leads to a stiffer EOS for the liquid core, but a lower core–crust transition density. The crossing point of the M – R curves with $x = 0$ and $x = -1$ is a result of this competition. It is clearly shown that with the PA the radius is larger at a fixed mass especially for the stiffer symmetry energy of $x = -1$. To better understand the role of the transition density in determining the M – R relation, we also made an additional test using the full MDI EOS but with the ρ_t obtained from using the PA. The results are shown with the dotted lines. They are very close to the results obtained consistently using the PA in calculating both the EOS and the transition density. Thus, the mass–radius relation, especially the radius, seems to be quite sensitive to the location of the inner edge. The small difference between the full EOS and its PA for the core (shown in panels (a) and (b) of Figure 2) has a negligible effect on the M – R relationship once the inner edge is fixed. These features can be seen more clearly in Figure 14 where the mass and radius are displayed separately as functions of the central energy density. Very similar masses are obtained independently of how the ρ_t was calculated for a given parameter x . However, the radii are appreciably different for the stiffer symmetry energy with $x = -1$ using the full EOS or its PA because of their different ρ_t values. Also, since the test case has the same ρ_t as the PA, it thus leads to the same radii as the PA for both $x = 0$ and $x = -1$.

5.8. The Crust Thickness and the Core Size of Neutron Stars

For a given neutron star of total mass M and radius R , what are the respective sizes of its core and crust? How do they depend on the stiffness of the symmetry energy? How do they depend on the neutron star mass M ? It is well known that the size of the neutron skin in heavy nuclei increases with increasing L as shown in Figure 7. How does the thickness of neutron star crusts depend on L ? These are among the interesting questions we shall discuss in this subsection. First, we display in Figure 15 the radial energy density profile for neutron stars of total mass $0.4 M_\odot$, $1.0 M_\odot$, and $1.4 M_\odot$ using the MDI interaction with $x = 0$ and $x = -1$, respectively. The inner edge separating the uniform core from the crust is indicated by the vertical dotted lines. The corresponding energy density ϵ_t is shown as the longitudinal dotted lines. It is very interesting to see

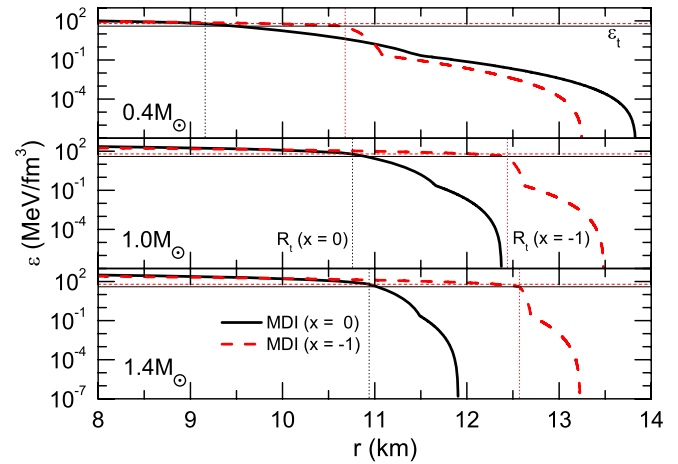


Figure 15. Radial energy density distribution of neutron stars, using the MDI interaction with $x = 0$ and $x = -1$, at total mass $0.4 M_\odot$, $1.0 M_\odot$, and $1.4 M_\odot$. The interface between the uniform and crust parts is indicated. R_t is the radius of the liquid core and ϵ_t is the energy density at the edge of the liquid core and the crust.

(A color version of this figure is available in the online journal.)

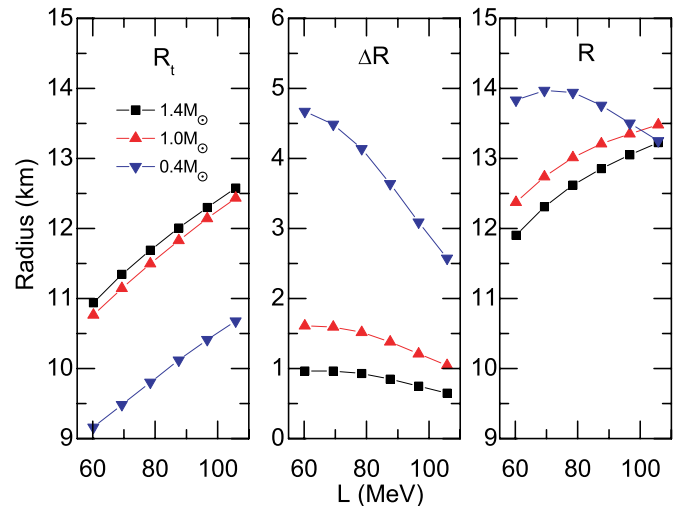


Figure 16. Whole radius R , the crust thickness ΔR , and the core radius R_t as functions of L at fixed total mass of $0.4 M_\odot$, $1.0 M_\odot$, and $1.4 M_\odot$, respectively. (A color version of this figure is available in the online journal.)

that the radius of the core increases while the thickness of the crust decreases with increasing neutron star mass M . The lighter neutron stars generally have thicker and more diffusive crusts due to the competition between the gravitational and nuclear forces. Moreover, this feature is independent of the symmetry energy used. It is also seen that the stiffer symmetry energy with $x = -1$ predicts a larger core but a thinner crust for a given mass M . More quantitatively, for a canonical neutron star of $M = 1.4 M_\odot$, the radius of the core is 10.89 km with $x = 0$ and 12.55 km with $x = -1$, and the thickness of the crust is 1.09 km with $x = 0$ and 0.72 km with $x = -1$, respectively. Therefore, with a softer symmetry energy, a light neutron star can have a big radius due to its very thick crust.

To study more systematically the effects of the symmetry energy, we show in Figure 16 the core radius R_t , the crust thickness ΔR , and the total radius R as functions of L for a fixed total mass of $0.4 M_\odot$, $1.0 M_\odot$, and $1.4 M_\odot$, respectively. It is seen that R_t increases almost linearly with increasing L . R_t also increases with increasing mass at fixed L . This is because the stiffer the symmetry energy is, the larger the contribution

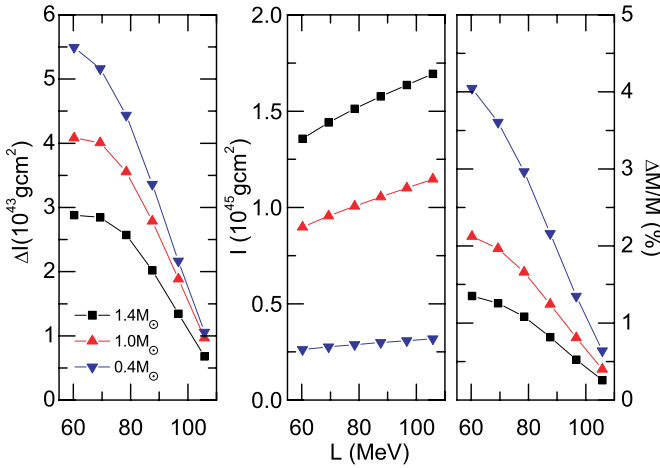


Figure 17. Crustal fraction of neutron mass $\Delta M/M$, the moment of inertia I of the whole star, and the crust contribution ΔI as a function of L at fixed total mass $0.4 M_{\odot}$, $1.0 M_{\odot}$, and $1.4 M_{\odot}$, respectively.

(A color version of this figure is available in the online journal.)

of the isospin asymmetric part of the pressure will be, which makes R_t larger. Moreover, ΔR decreases with increasing L especially for light neutron stars as the transition density decreases with increasing L . As the thickness of the crust ΔR and the core radius R_t depend oppositely on L , the total radius $R = R_t + \Delta R$ of the neutron star may show a complicated dependence on L . We stress here that this is the result of a competition between the repulsive nuclear pressure dominated by the symmetry energy contribution and the gravitational binding. Interestingly, it is often mentioned that the crust of neutron stars bears some analogy with the neutron skin of heavy nuclei. However, they show completely opposite dependences on L : namely, the size of the neutron skin usually increases with increasing L as a result of the competition between the nuclear surface tension and the pressure difference of neutrons and protons, while the thickness of neutron star crusts decreases with increasing L as a result of the competition between the nuclear pressure and the gravitational binding.

5.9. The Crustal Fractions of Neutron Star Masses and Moments of Inertia

What is the crustal fraction $\Delta M/M$ of the total mass, and how does it depend on the symmetry energy? Since the mass is simply the integration of the energy density, from the profile of the energy density shown in Figure 15 we expect $\Delta M/M$ and $\Delta R/R$ to have very similar dependences on L . Shown in the right panel of Figure 17 is $\Delta M/M$. The fractional mass of the crust decreases with increasing L at a fixed total mass, and it decreases with increasing total mass at a fixed value of L . The moment of inertia is determined by the distribution of the energy density. From the middle panel, it is seen that the total moment of inertia increases with increasing mass at a fixed value of L and increases with increasing L at a fixed total mass. The dependence on L is relatively weak especially for the light neutron stars. However, the crust contribution of the moment of inertia varies much more quickly with L . It decreases with increasing neutron star mass at a fixed value of L and decreases with increasing L at a fixed total mass. These are all consistent with the behaviors of the fractional mass and size of the crust.

The crustal fraction of the moment of inertia $\Delta I/I$ is particularly interesting as it can be inferred from observations

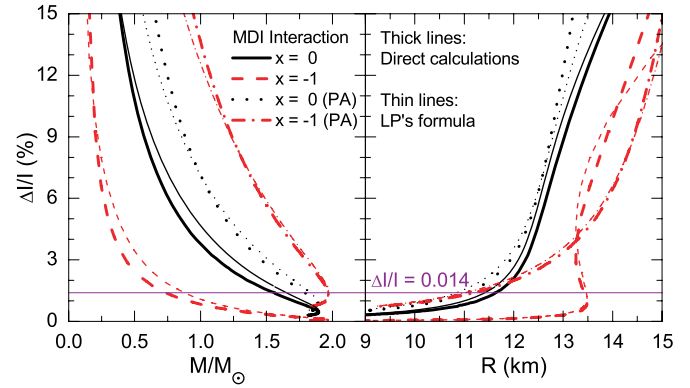


Figure 18. Relation between the crustal fraction of the moment of inertia and the total mass or the radius of neutron stars, using the MDI interaction with $x = 0$ and $x = -1$. The results of the PA or exact method from direct calculation or LP's formula are shown for comparison, and the constraint of $\Delta I/I$ is also indicated.

(A color version of this figure is available in the online journal.)

of pulsar glitches, the occasional disruptions of the otherwise extremely regular pulsations from magnetized, rotating neutron stars. It can be expressed approximately as (Lattimer & Prakash 2000, 2001, 2007)

$$\frac{\Delta I}{I} = \frac{28\pi P_t R^3 (1 - 1.67\xi - 0.6\xi^2)}{3Mc^2 \xi} \times \left[1 + \frac{2P_t(1 + 5\xi - 14\xi^2)}{\rho_t mc^2 \xi^2} \right]^{-1}, \quad (93)$$

where m is the mass of baryons and $\xi = GM/Rc^2$. A numerical verification of this formula is useful. Predictions of this formula (thin lines) are compared in Figure 18 with our direct numerical calculations (thick lines). Very interestingly, the analytical formula reproduces very well our results from direct numerical calculations using both the full EOS and its PA. Comparing calculations using the full EOS and its PA, one sees clearly big differences, again due to the corresponding differences in the transition density. For instance, using either the direct numerical calculation or Equation (93), at a fixed total mass M $\Delta I/I$ increases using the full EOS while it decreases using the PA when the parameter x is changed from $x = -1$ to $x = 0$. As was stressed by Lattimer & Prakash (2000, 2001), $\Delta I/I$ depends sensitively on the symmetry energy at subsaturation densities through P_t and ρ_t , but there is no explicit dependence upon the EOS at higher densities.

Experimentally, the crustal fraction of the moment of inertia has been constrained as $\Delta I/I > 0.014$ from studying the glitches of the Vela pulsar (Link et al. 1999). As indicated in Figure 18 this limits the masses and radii of the neutron star. For example, from Figure 18 it is indicated that the maximum mass is about $1.57 M_{\odot}$ ($0.73 M_{\odot}$) while its minimum radius is about 11.6 (13.4) km for the MDI interaction with $x = 0$ ($x = -1$) if the dynamical method is used to determine P_t and ρ_t . We note here that the very small mass for the Vela pulsar constrained by this condition using the MDI with $x = -1$ is due to the associated small transition density and pressure. Combining the observational constraint of $\Delta I/I > 0.014$ with the upper bounds of $\rho_t = 0.065 \text{ fm}^{-3}$ and $P_t = 0.26 \text{ MeV fm}^{-3}$ inferred from heavy-ion reactions, we can obtain a minimum radius of $R \geq 4.7 + 4.0M/M_{\odot}$ km for the Vela pulsar. This limit is indicated by the solid squares in Figure 13. According to this constraint, the radius of the Vela pulsar is predicted to

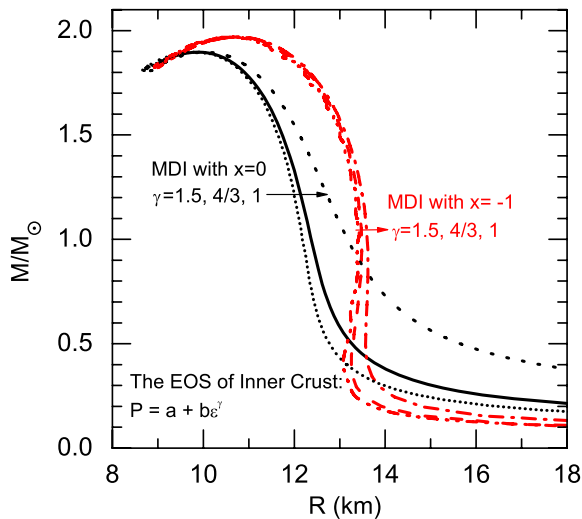


Figure 19. The M - R relation of static neutron stars from the full MDI EOS with $x = 0$ and $x = -1$. Different values of the polytropic index γ in $P = a + b\epsilon^\gamma$ for the inner crust EOS, i.e., $\gamma = 1.5, 4/3$, and 1 , have been used.

(A color version of this figure is available in the online journal.)

exceed 10.5 km should it have a mass of $1.4 M_\odot$. It is worth mentioning that a constraint of $R \geq 3.6 + 3.9M/M_\odot$ km for this pulsar (see the open squares in Figure 13) has been derived by previously Link et al. (1999) using $\rho_t = 0.075 \text{ fm}^{-3}$ and $P_t = 0.65 \text{ MeV fm}^{-3}$. The difference between this and our prediction is due to the different ρ_t and P_t .

5.10. The Inner Crust EOS Dependence of Neutron Star Properties

As discussed in Equation (91) of Section 5.6, we have adopted the polytropic EOS of $P = a + b\epsilon^\gamma$ with $\gamma = 4/3$ for the inner crust in the above calculations. This particular polytropic EOS has been extensively used for studying the inner crust in the literature (Link et al. 1999; Lattimer & Prakash 2000, 2001; Carriere et al. 2003). However, due to the complexity of the inner crust, its EOS is rather uncertain (Negele & Vautherin 1973). Thus, it would be interesting to investigate how our results may be sensitive to the polytropic index γ .

First, let us see how the polytropic index affects the mass and radius of a neutron star. Shown in Figure 19 is the M - R relation obtained using the full MDI EOS with $x = 0$ and $x = -1$ with three different values of the polytropic index γ , i.e., $\gamma = 1.5, 4/3$, and 1 . It is seen that the polytropic index has very little effect on the mass of neutron stars. On the other hand, it is interesting to see that the neutron star radius increases significantly with decreasing polytropic index's γ especially for the softer symmetry energy ($x = 0$). This is due to the change of the crust thickness from varying the inner crust EOS. The observed symmetry energy dependence of the polytropic index's effects on the neutron star radius can be easily understood since the stiffer symmetry energy leads to a thinner thickness of the crust as shown in Figure 16 and thus less sensitivity to the variation of the inner crust EOS. Our results thus indicate that for softer symmetry energies an accurate inner crust EOS is important for the precise determination of the neutron star radius.

In order to see the inner crust EOS dependence of the crustal fraction of the moment of inertia $\Delta I/I$, we show in Figure 20 $\Delta I/I$ as functions of the total mass and the radius of neutron stars from the full MDI EOS with $x = 0$ and $x = -1$ using

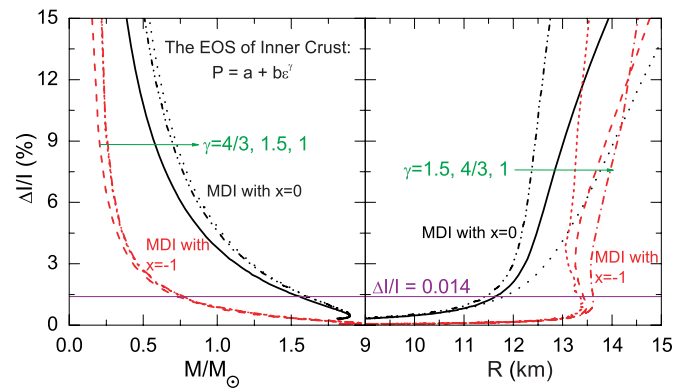


Figure 20. The relation between the crustal fraction of the moment of inertia and the total mass or the radius of neutron stars using the MDI interaction with $x = 0$ and $x = -1$. Different values of the polytropic index γ in $P = a + b\epsilon^\gamma$ for the inner crust EOS, i.e., $\gamma = 1.5, 4/3$, and 1 , have been used. The constraint of $\Delta I/I$ is also indicated.

(A color version of this figure is available in the online journal.)

$\gamma = 1.5, 4/3$, and 1 . Noting the very weak dependence of the neutron star mass on the index γ , we can see clearly from the left panel of Figure 20 that $\Delta I/I$ is not so sensitive to the variation of the inner crust EOS, especially for stiffer symmetry energies. We notice here that the pronounced γ index dependence of $\Delta I/I$ as a function of the neutron star radius is due to the fact that the neutron star radius depends significantly on the index γ as shown in Figure 19, especially for the softer symmetry energy ($x = 0$).

Also indicated in Figure 20 is the constraint of $\Delta I/I$ from studying the glitches of the Vela pulsar (Link et al. 1999). It is very interesting to see that the neutron star mass and radius at $\Delta I/I = 0.014$ exhibit a very weak dependence on the polytropic index γ . This nice feature implies that the obtained constraint on the minimum radius of $R \geq 4.7 + 4.0M/M_\odot$ km for the Vela pulsar in the present work is not sensitive to the inner crust EOS and still holds. Moreover, we can see from Figure 20 that the robustness of the constraint $R \geq 4.7 + 4.0M/M_\odot$ km against the variation of the inner crust EOS is actually due to the very small value of $\Delta I/I$ for the Vela pulsar. For higher values of $\Delta I/I$, on the contrary, the constraint will depend significantly on the inner crust EOS.

6. SUMMARY

In summary, we first analyzed the relationship between the well established dynamical and thermodynamical methods for locating the inner edge separating the uniform liquid core from the solid crust in neutron stars. It is shown analytically that the thermodynamical method corresponds to the long-wavelength limit of the dynamical one when the Coulomb interaction is neglected. Moreover, it is shown that the results obtained from using the full expression of the EOS for a given interaction are very similar for the two methods. However, the widely used parabolic approximation to the EOS of asymmetric nuclear matter leads systematically to significantly higher core-crust transition densities and pressures, especially for stiffer symmetry energy functionals, regardless of the specific method used in calculating the transition density. Our results thus indicate that one can hardly obtain the accurate transition density without knowing the complete EOS and may introduce a huge error by assuming a priori that the EOS is parabolic in isospin asymmetry for a given interaction. Based on systematical calculations using the modified Gogny force (MDI interaction)

and 51 selected Skyrme interactions widely used in the literature, it is shown that the transition density and pressure are very sensitive to the density dependence of the nuclear symmetry energy. We also systematically investigated several properties of the neutron star crust. We found that the thickness, fractional mass, and moment of inertia of the neutron star crust are all very sensitive to the slope parameter L of the nuclear symmetry energy through the transition density ρ_t and the results depend on whether one uses the full EOS or its parabolic approximation. Therefore, accurate knowledge on the nuclear symmetry energy at subsaturation densities is required to fully understand the properties of neutron star crusts.

Using the MDI EOS of neutron-rich nuclear matter constrained by the recent isospin diffusion data from heavy-ion reactions in the same subsaturation density range as the neutron star crust, the transition density and pressure at the inner edge of neutron star crusts are limited to $0.040 \text{ fm}^{-3} \leq \rho_t \leq 0.065 \text{ fm}^{-3}$ and $0.01 \text{ MeV fm}^{-3} \leq P_t \leq 0.26 \text{ MeV fm}^{-3}$, respectively. The constrained range of the transition density is significantly below the fiducial value of $\rho_t \approx 0.08 \text{ fm}^{-3}$ often used in the literature and the estimate of $0.5 < \rho_t/\rho_0 < 0.7$ made previously within the thermodynamical approach using the parabolic approximation of the EOS while the constrained range of P_t is also significantly less than the fiducial value of $P_t \approx 0.65 \text{ MeV fm}^{-3}$ often used in the literature. The newly constrained transition density and pressure together with the condition $\Delta I/I > 0.014$ for the crustal fraction of the moment of inertia extracted from studying glitches of the Vela pulsar allow us to set a new limit on the radius of the Vela pulsar, i.e., $R \geq 4.7 + 4.0M/M_\odot$. This is significantly different from the previous estimate and thus puts a new constraint on the mass–radius relation of neutron stars.

Finally, it is worth noting that in the present work we have only considered the nonaccreting crusts of cold, nonrotating nucleonic neutron stars. In the next step, we plan to extend the study to accreting neutron stars. It will be especially interesting to investigate how the finite temperature, the strong magnetic field and neutrino trapping may affect the transition density and pressure reported here. Moreover, there are still many interesting issues regarding the neutron star crust, such as its composition, thermal, transport and mechanical properties that are important for a better understanding of the structure and evolution of protoneutron stars, the X-ray bursts and the emission of gravitational waves from neutron stars. More information from terrestrial nuclear reactions especially those induced by radioactive beams will certainly contribute to resolving these issues.

This work was supported in part by the National Natural Science Foundation of China under grant nos. 10575071, 10675082, and 10874111, MOE of China under project NCET-05-0392, Shanghai Rising-Star Program under grant no. 06QA14024, the SRF for ROCS, SEM of China, the National Basic Research Program of China (973 Program) under contract no. 2007CB815004, the US National Science Foundation under grant no. PHY-0652548, PHY-0757839 and PHY-0457265, the Welch Foundation under grant no. A-1358, the Research Corporation under Award No. 7123 and the Texas Coordinating Board of Higher Education Award No. 003565-0004-2007.

REFERENCES

- Arponen, J. 1972, *Nucl. Phys. A*, **191**, 257
- Avancini, S. S., et al. 2008, *Phys. Rev. C*, **78**, 015802
- Avancini, S. S., et al. 2009, *Phys. Rev. C*, **79**, 035804
- Baym, G., Pethick, C. J., & Sutherland, P. 1971a, *ApJ*, **170**, 299
- Baym, G., Bethe, H. A., & Pethick, C. J. 1971b, *Nucl. Phys. A*, **175**, 225
- Bombaci, I., & Lombardo, U. 1991, *Phys. Rev. C*, **44**, 1892
- Bombaci, I. 2001, in *Isospin Physics in Heavy Ion Collisions at Intermediate Energies*, ed. B.-A. Li & W. Udo Schroder (New York: Nova Science Publishers), 35
- Brack, M., Guet, C., & Hakansson, H.-B. 1985, *Phys. Rep.*, **123**, 275
- Brown, B. A. 1998, *Phys. Rev. C*, **58**, 220
- Brown, B. A. 2000, *Phys. Rev. Lett.*, **85**, 5296
- Burrows, A., Reddy, S., & Thompson, T. A. 2006, *Nucl. Phys. A*, **777**, 356
- Carriere, J., Horowitz, C. J., & Piekarewicz, J. 2003, *ApJ*, **593**, 463
- Chabanat, E., Bonche, E., Haensel, E., Meyer, J., & Schaeffer, R. 1997, *Nucl. Phys. A*, **627**, 710
- Chamel, N., Goriely, S., & Pearson, J. M. 2008, *Nucl. Phys. A*, **812**, 72
- Chamel, N., & Haensel, P. 2008, *Living Rev. Relat.*, **11**, 10
- Chen, L. W., Zhang, F. S., Lu, Z. H., Li, W. F., Zhu, Z. Y., & Ma, H. R. 2001, *J. Phys. G: Nucl. Part. Phys.*, **27**, 1799
- Chen, L. W., Ko, C. M., & Li, B. A. 2005a, *Phys. Rev. Lett.*, **94**, 032701
- Chen, L. W., Ko, C. M., & Li, B. A. 2005b, *Phys. Rev. C*, **72**, 064309
- Chen, L. W., Ko, C. M., & Li, B. A. 2007, *Phys. Rev. C*, **76**, 054316
- Chomaz, Ph., Colonna, M., & Randrup, J. 2004, *Phys. Rep.*, **389**, 263
- Das, C. B., Gupta, S. D., Gale, C., & Li, B.-A. 2003, *Phys. Rev. C*, **67**, 034611
- Das, C. B., Das Gupta, S., Lynch, W. G., Mekjian, A. Z., & Tsang, M. B. 2005, *Phys. Rep.*, **406**, 1
- Dieperink, A. E. L., et al. 2003, *Phys. Rev. C*, **68**, 064307
- Douchin, F., & Haensel, P. 2000, *Phys. Lett. B*, **485**, 107
- Douchin, F., & Haensel, P. 2001, *A&A*, **380**, 151
- Ducoin, C., Chomaz, Ph., & Gulminelli, F. 2007, *Nucl. Phys. A*, **789**, 403
- Duncan, R. C. 1998, *ApJ*, **498**, L45
- Friedrich, J., & Reinhard, P.-G. 1986, *Phys. Rev. C*, **33**, 335
- Furnstahl, R. J. 2002, *Nucl. Phys. A*, **706**, 85
- Gale, C., Bertsch, G. F., & Das Gupta, S. 1987, *Phys. Rev. C*, **35**, 1666
- Gale, C., Welke, G. M., Prakash, M., Lee, S. J., & Das Gupta, S. 1990, *Phys. Rev. C*, **41**, 1545
- Gögelein, P., van Dalen, E. N. E., Fuchs, C., & Muther, H. 2008, *Phys. Rev. C*, **77**, 025802
- Goriely, S., et al. 2003, *Phys. Rev. C*, **68**, 054325
- Goriely, S., et al. 2005, *Nucl. Phys. A*, **750**, 425
- Goriely, S., Samyn, M., & Pearson, J. M. 2006, *Nucl. Phys. A*, **773**, 279
- Goriely, S., Samyn, M., & Pearson, J. M. 2007, *Phys. Rev. C*, **75**, 064312
- Goriely, S., & Pearson, J. M. 2008, *Phys. Rev. C*, **77**, 031301
- Hashimoto, M., Seki, H., & Yamada, M. 1984, *Prog. Theor. Phys.*, **71**, 320
- Hempel, M., & Schaffner-Bielich, J. 2008, *J. Phys. G*, **35**, 014043
- Horowitz, C. J., & Piekarewicz, J. 2001a, *Phys. Rev. Lett.*, **86**, 5647
- Horowitz, C. J., & Piekarewicz, J. 2001b, *Phys. Rev. C*, **64**, 062802
- Horowitz, C. J., Pollock, S. J., Souder, P. A., & Michaels, R. 2001, *Phys. Rev. C*, **63**, 025501
- Horowitz, C. J., et al. 2004a, *Phys. Rev. C*, **69**, 045804
- Horowitz, C. J., et al. 2004b, *Phys. Rev. C*, **70**, 065806
- Horowitz, C. J. talk at the World Consensus Initiative, 12–16 February 2005, College Station, Texas, USA (<http://cyclotron.tamu.edu/wci3/>)
- Horowitz, C. J. 2006, *Eur. Phys. J. A*, **30**, 303
- Iida, K., & Sato, K. 1997, *ApJ*, **477**, 294
- Krastev, P. G., & Li, B. A. 2007, *Phys. Rev. C*, **76**, 055804
- Krastev, P. G., Li, B. A., & Worley, A. 2008a, *ApJ*, **676**, 1170
- Krastev, P. G., Li, B. A., & Worley, A. 2008b, *Phys. Lett. B*, **668**, 1
- Kubis, S. 2004, *Phys. Rev. C*, **70**, 065804
- Kubis, S. 2007, *Phys. Rev. C*, **76**, 035801
- Lattimer, J. M., & Prakash, M. 2000, *Phys. Rep.*, **333**, 121
- Lattimer, J. M., & Prakash, M. 2001, *ApJ*, **550**, 426
- Lattimer, J. M., & Prakash, M. 2004, *Science*, **304**, 536
- Lattimer, J. M., & Prakash, M. 2007, *Phys. Rep.*, **442**, 109
- Li, B. A., & Ko, C. M. 1997, *Nucl. Phys. A*, **618**, 498
- Li, B. A., & Chen, L. W. 2005, *Phys. Rev. C*, **72**, 064611
- Li, B. A., & Steiner, A. W. 2006, *Phys. Lett. B*, **642**, 436
- Li, B. A., Chen, L. W., Ma, H. R., Xu, J., & Yong, G. C. 2007, *Phys. Rev. C*, **76**, 051601
- Li, B. A., Chen, L. W., & Ko, C. M. 2008, *Phys. Rep.*, **464**, 113
- Link, B., Epstein, R. I., & Lattimer, J. M. 1999, *Phys. Rev. Lett.*, **83**, 3362
- Lorenz, C. P., Ravenhall, D. G., & Pethick, C. J. 1993, *Phys. Rev. Lett.*, **70**, 379
- Lynch, W. G., et al. 2009, arXiv:0901.0412
- Margueron, J., & Chomaz, P. 2003, *Phys. Rev. C*, **67**, 041602
- Morrison, I. A., Baumgarte, T. W., Shapiro, S. L., & Pandharipande, V. R. 2004, *ApJ*, **617**, 135
- Moustakidis, Ch. C. 2007, *Phys. Rev. C*, **76**, 025805
- Müller, H., & Serot, B. D. 1995, *Phys. Rev. C*, **52**, 2072
- Negele, J. W., & Vautherin, D. 1973, *Nucl. Phys. A*, **207**, 298

- Oppenheimer, J., & Volkoff, G. 1939, *Phys. Rev.*, **55**, 374
- Oyamatsu, K. 1993, *Nucl. Phys. A*, **561**, 431
- Oyamatsu, K., & Iida, K. 2007, *Phys. Rev. C*, **75**, 015801
- Pethick, C. J., & Ravenhall, D. G. 1995, *Ann. Rev. Nucl. Part. Sci.*, **45**, 429
- Pethick, C. J., Ravenhall, D. G., & Lorenz, C. P. 1995, *Nucl. Phys. A*, **584**, 675
- Piekraewicz, J. 2007, *Phys. Rev. C*, **76**, 064310
- Prakash, M., Kuo, T. T. S., & Das Gupta, S. 1988, *Phys. Rev. C*, **37**, 2253
- Rabhi, A., Providência, C., & Da Providência, J. 2009, *Phys. Rev. C*, **79**, 015804
- Ravenhall, D. G., Pethick, C. J., & Wilson, J. R. 1983, *Phys. Rev. Lett.*, **50**, 2066
- Ruster, S. B., Hempel, M., & Schaffner-Bielich, J. 2006, *Phys. Rev. C*, **73**, 035804
- Rutledge, R. E., et al. 2006, *ApJ*, **580**, 413
- Samyn, M., et al. 2002, *Nucl. Phys. A*, **700**, 142
- Samyn, M., Goriely, S., & Pearson, J. M. 2003, *Nucl. Phys. A*, **725**, 69
- Samyn, M., et al. 2004, *Phys. Rev. C*, **70**, 044309
- Samyn, M., Goriely, S., & Pearson, J. M. 2005, *Phys. Rev. C*, **72**, 044316
- Shetty, D., Yennello, S. J., & Souliotis, G. A. 2007, *Phys. Rev. C*, **75**, 034602
- Siemens, P. J. 1983, *Nature*, **305**, 410
- Steiner, A. W., Prakash, M., Lattimer, J. M., & Ellis, P. J. 2005a, *Phys. Rep.*, **410**, 325
- Steiner, A. W., & Li, B. A. 2005b, *Phys. Rev. C*, **72**, 041601
- Steiner, A. W. 2006, *Phys. Rev. C*, **74**, 045808
- Steiner, A. W. 2008, *Phys. Rev. C*, **77**, 035805
- Stone, J. R., Miller, J. C., Koncewicz, R., Stevenson, P. D., & Strayer, M. R. 2003, *Phys. Rev. C*, **68**, 034324
- Stone, J. R., & Reinhard, P.-G. 2007, *Prog. Part. Nucl. Phys.*, **58**, 587
- Todd-Rutel, B. G., & Piekarewicz, J. 2005, *Phys. Rev. Lett.*, **95**, 122501
- Tsang, M. B., et al. 2001, *Phys. Rev. Lett.*, **86**, 5023
- Tsang, M. B., et al. 2004, *Phys. Rev. Lett.*, **92**, 062701
- Tsang, M. B., et al. 2009, *Phys. Rev. Lett.*, **102**, 122701
- van Dalena, E. N. E., Fuchs, C., & Faessler, A. 2007, *Eur. Phys. J. A*, **31**, 29
- Watanabe, G., Maruyama, T., Sato, K., Yasuoka, K., & Ebisuzaki, T. 2005, *Phys. Rev. Lett.*, **94**, 031101
- Welke, G. M., Prakash, M., Kuo, T. T. S., Das Gupta, S., & Gale, C. 1988, *Phys. Rev. C*, **38**, 2101
- Worley, A., Krastev, P. G., & Li, B. A. 2008a, *ApJ*, **685**, 390
- Worley, A., Krastev, P. G., & Li, B. A. 2008b, arXiv:0812.0408
- Xu, J., Chen, L. W., Li, B. A., & Ma, H. R. 2007a, *Phys. Rev. C*, **75**, 014607
- Xu, J., Chen, L. W., Li, B. A., & Ma, H. R. 2007b, *Phys. Lett. B*, **650**, 348
- Xu, J., Chen, L. W., Li, B. A., & Ma, H. R. 2008, *Phys. Rev. C*, **77**, 014302
- Xu, J., Chen, L. W., Li, B. A., & Ma, H. R. 2009, *Phys. Rev. C*, **79**, 035802
- Zhang, F. S., & Chen, L. W. 2001, *Chin. Phys. Lett.*, **18**, 142
- Zuo, W., et al. 2004, *Phys. Rev. C*, **69**, 064001